CB-Note 311

TECHNICAL REPORT : ANTIPROTON-PROTON ANNIHILATION AT REST INTO $K_S^0 K_S^0 \pi^0$ and $K_S^0 K_S^0 \eta$

Oliver Cramer
University of Munich

Munich, 27 January 1997

Abstract

$1.6 \cdot 10^6$ events taken in October 1993 with a K_S^0-trigger (no hit in PWC 1, at least to hits in layers 20 and 21) are selected and the acceptance corrected Dalitz plots for the final states $K_S^0 K_S^0 \pi^0$ and $K_S^0 K_S^0 \eta$ are produced. 10046 events of $K_S^0 K_S^0 \pi^0$with one charged K_S^0-decay have been found and 5782 events with both K_S^0 decaying into $\pi^+ \pi^-$. Due to limited phase space the statistics in the final state $K_S^0 K_S^0 \eta$ is very low (370/171 events). The Dalitz plots of both channels are almost free of background and the acceptance (in particular the strong trigger effect) is well understood.

The partial wave analysis was done for the 10046 $K_S^0 K_S^0 \pi^0$-events with one neutral K_S^0-decay. Two scalar resonances in $K\overline{K}$are required, the $f_0(1370)$ ($M = 1439^{+10}_{-20}\ MeV/c^2, \Gamma = 360 \pm 50\ MeV/c^2$) and the $f_0(1500)$ ($M = 1515 \pm 5\ MeV/c^2, \Gamma = 88^{+15}_{-5}\ MeV/c^2$) which are parametrized in the fit in terms of a 1x1 K-matrix.

The $a_0(1450)$ can neither be confirmed nor excluded, equally good fits are obtained with a contribution between 0 and 25 %. The effect of the $a_0(1450)$-contribution on the f_0-poles and its influence on $\gamma^2_{K\overline{K}}/\gamma^2_{\pi\pi}$ has been studied.

A clear signal at the $K\overline{K}$-threshold is observed, but the contributions of $f_0(975)$ and $a_0(980)$ cannot be dissolved from the $K_S^0 K_S^0 \pi^0$-channel alone.

The $(K\pi)_S$-wave has to be fitted with two different production strengths to $p\overline{p}$ for the pole and for the effective range term. Its contribution is weak but it is very important for the description of the data due to its strong interference with the $(K\overline{K})_S$-wave. Fits with a simplified parametrization using the pole term only give similar results and are much easier to handle in practice.

The results of intensities and production rates for all resonant states are compatible with results from other channels except the prediction of the $a_2(1320)$-intensity from the $\eta\pi^0\pi^0$- channel.

Contents

List of Figures

List of Tables

Chapter 1

Data taking and data selection

1.1 The K_S^0-Trigger of the 10/93 run

In October 1993 we have recorded more than 1.6 million events using the following trigger conditions :

- no signal in PWC 1
- at least two hits in layer 20 and 21 of the JDC

The first trigger step rejects those 96% of events where charged particles are produced at the primary vertex of the $p\overline{p}$ -annihilation, the second step then rejects the all neutral events.

Hence this trigger selects final states where one or more K_S^0, decaying into π^+ π^- outside of PWC 1, and no other charged particle is produced. In tab. 1.1 the acceptances of this trigger are given for some important channels, with one respectively two charged K_S^0-decays per event.

In fig. 1.1 possible topologies of K_S^0-decays are shown. The dotted lines represent the K_S^0 which are invisible for the detector and the full lines the charged pions. A decay like in *a* is accepted by the trigger, but *b* and *c* are not. In *b* the decay vertex is outside the PWC 1 but one charged pion is boosted backwards and hits the layers of the inner PWC. In *c* the opening angle of one pion with the z-axis is so small that it gives no signal in the outer layers of the JDC.

channel	$K_S^0 K_S^0 \pi^0$	$K_S^0 K_S^0 \eta$	$K_S^0 K_S^0 \omega$	$K_S^0 K_S^0$	$K_S^0 K_S^0 \pi^0 \pi^0$
1 charged and 1 neutral K_S^0-decay	29,3 %	17,8 %	5,3 %	45,5 %	19.8 %
2 charged and 0 neutral K_S^0-decays	9,2 %	3,1 %	0,3 %	22,3 %	4.2 %

Table 1.1: *Probabilities for different $K_S^0 K_S^0 X$-channels, that all charged tracks are produced at least 2.5 cm from the z-axis. Results are obtained by a pure phase space simulation using GENBOD [2]*

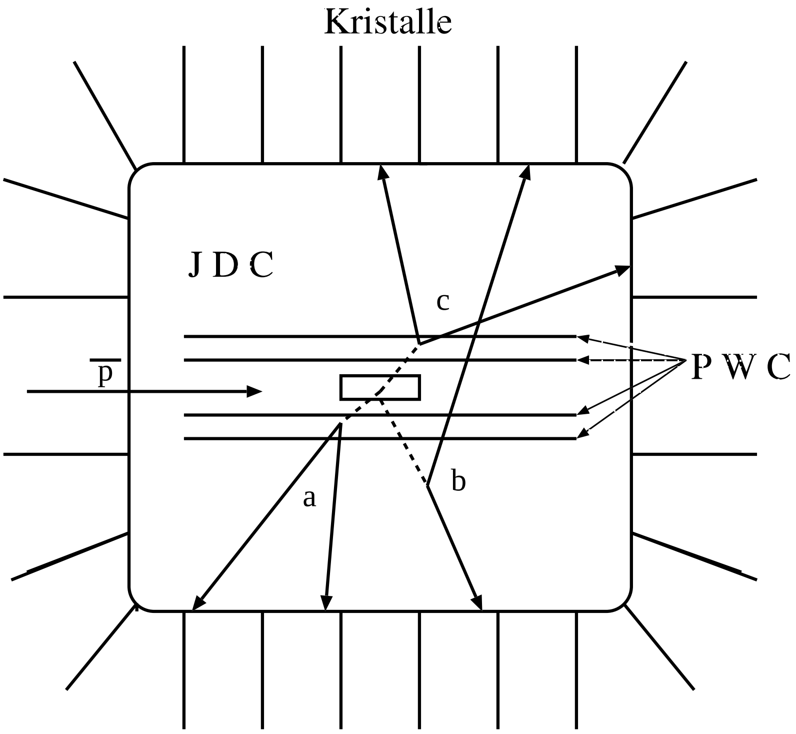

Figure 1.1: *The K_S^0-trigger : dotted lines refer to K_S^0, full lines to the charged pions. Topology* **a** *is accepted by the trigger,* **b** *(> 0 hits in PWC 1) and* **c** *(< 2 hits in JDC layer 20 or 21) are rejected.*

As shown in fig. 1.2 the data taking was affected by some problems at the beginning of the run period. Fig. 1.2a shows the z-component of the reconstructed vertex for events with exactly two charged tracks. A small peak can be seen at the position of the silicon entrance counters and many annihilations far behind the target.

The latter ones can easily be cut out in the data selection, the peak in the silicon counters will disappear during the analysis. In fig. 1.2b we can see that these problems have been solved during the run period.

Monte Carlo simulation

In order to reduce computing time (see tab. 1.1) events are only fully generated if the distance between the charged K_S^0-decay and the z-axis is at least 2.5 cm. Before the simulation of the tracking of a particle through the detector is performed the information about its four-vector and its life time is provided in the routine GLTRAC of GEANT and a fast decision can be made if the complete event shall be generated or if one wants to switch immediately to the next event.

In order to justify this method 150 000 events with charged K_S^0 decays inside the PWC 1 have been generated and only less than 10^{-3} of them fulfilled the trigger conditions. This is mainly due to the high efficiency of the PWC.

Software versions

In the October 1993 run 1 665 132 events have been recorded with the K_S^0-trigger, 1 605 571 show indeed no signal in PWC 1 and at least two hits in layers 20 and 21 of the JDC. For the reconstruction of these events the following software versions have been used :

- CBOFF 1.30/05 [3]
- LOCATER 2.01/06 [4]
- GTRACK 1.36/00 [5]
- BCTRAK 2.01/06 [6]
- CBKFIT 3.09/00 [7]
- CCDBCB 2.04/04 [8]

The Monte Carlo simulation was performed with the version 3.21/04 of GEANT [9] and CBGEANT 5.00/00 [10] and [11]. For the simulation of the hadronic interactions of the charged pions in the crystals the FLUKA option [12] [13] has been applied.

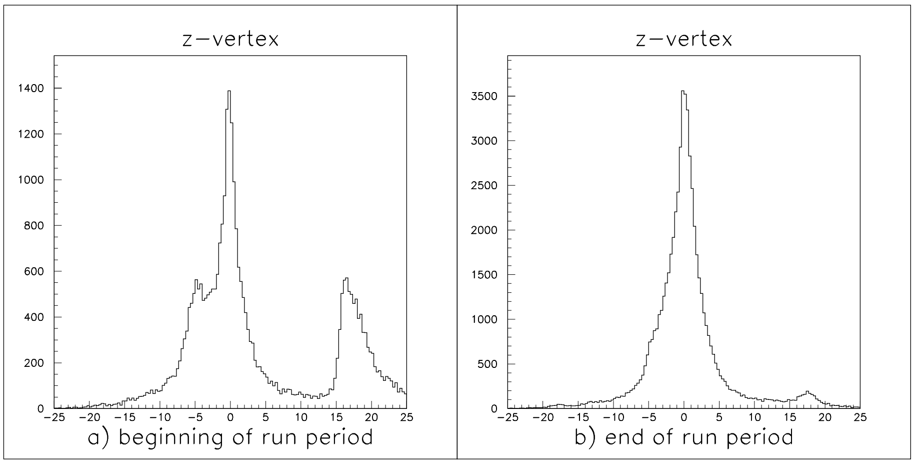

Figure 1.2: **a** *shows that at the beginning of data taking many events with annihilations in the entrance counters and far behind the target have been recorded. This could be improved later (***b***).*

1.2 The decay $K_S^0 \longrightarrow \pi^+ \pi^-$

Number of charged tracks

The selection of the final state allows one and two charged K_S^0-decays in each event :

$$p\overline{p} \rightarrow K_S^0(\rightarrow \pi^+ \pi^-) K_S^0(\rightarrow \pi^0 \pi^0) \pi^0 \tag{1.1}$$

$$p\overline{p} \rightarrow K_S^0(\rightarrow \pi^+ \pi^-) K_S^0(\rightarrow \pi^+ \pi^-) \pi^0 \tag{1.2}$$

Therefore all events with exactly two or four charged tracks are selected.

The secondary vertices

In the reconstruction the TCVER3 routine of LOCATER was used which is best suited if secondary vertices from decays like $K_S^0 \rightarrow \pi^+ \pi^-$ have to be found [14].

- Exactly one respectively two secondary vertices are required for events of type (1.1) respectively (1.2)
- All events with vertices far behind the target are rejected by a cut on the z-component of the secondary vertices : $z_V < 10\ cm$ (fig. 1.2 a).
- Not all of the reconstructed vertices are found outside the PWC 1. A large amount of data shows vertices much closer to the z-axis (fig. 1.3a), but Monte Carlo data indicate that most of these events are coming from background channels. In case a

secondary vertex is found to be closer than 2.5 cm from the z-axis the event will be rejected.

Secondary vertices which are found close to the origin are mainly due to γ-conversions into e^+e^- leading to a very small opening angle between the arising tracks. In the reconstruction the electrons are assumed to have the mass of a pion, hence the invariant mass of the e^+e^--pair becomes two times the pion mass. Fig. 1.3b and c show that charged pairs with two times the pion mass are indeed correlated to a small xy-vertex component and to a small opening angle.

It is evident that these entries correspond to e^+e^--pairs with such a small opening angle that the reconstruction of the correct secondary vertex failed and it is instead found to be zero.

Opening angle between charged tracks

Fig. 1.3c shows that the cosinus of the opening angle between the two charged tracks coming from the decay $K^0_S \to \pi^+ \, \pi^-$ is always smaller than 0.75, therefore all events with $cos(\pi^+, \pi^-) > 0.75$ will be rejected.

1.3 The photons in the calorimeter

Number of PEDs

The standard golden-γ cuts have been used for the definition of a PED.

The two pions of the neutral K^0_S-decay and the primary pion decay with 98.80 % [1] into two gammas. So we expect two respectively six PEDs which are not correlated with a charged track.

Hadronic splitoffs are identified by TAXI [22] and the electromagnetic splitoffs by DOLBY-C [21]. The four-vectors of the hadronic splitoffs are not added to the total energy and total momentum of the event, because they are included in the four-momentum measurement of their parent charged track in the JDC.

In addition the kinematic fit will be used as a further option to identify splitoffs (analogous to USDROP, see chap. 1.4), therefore all events with 2,3,6 and 7 PEDs are accepted at this stage.

Total energy and crystal type 13

A wide cut on the total energy ($1.55 \; GeV < E_{tot} < 2.20 \; GeV$) was applied which rejects among others events from channels involving $K^0_S K^0_L$.

Finally all events with PEDs in crystal type 13 are rejected as usual.

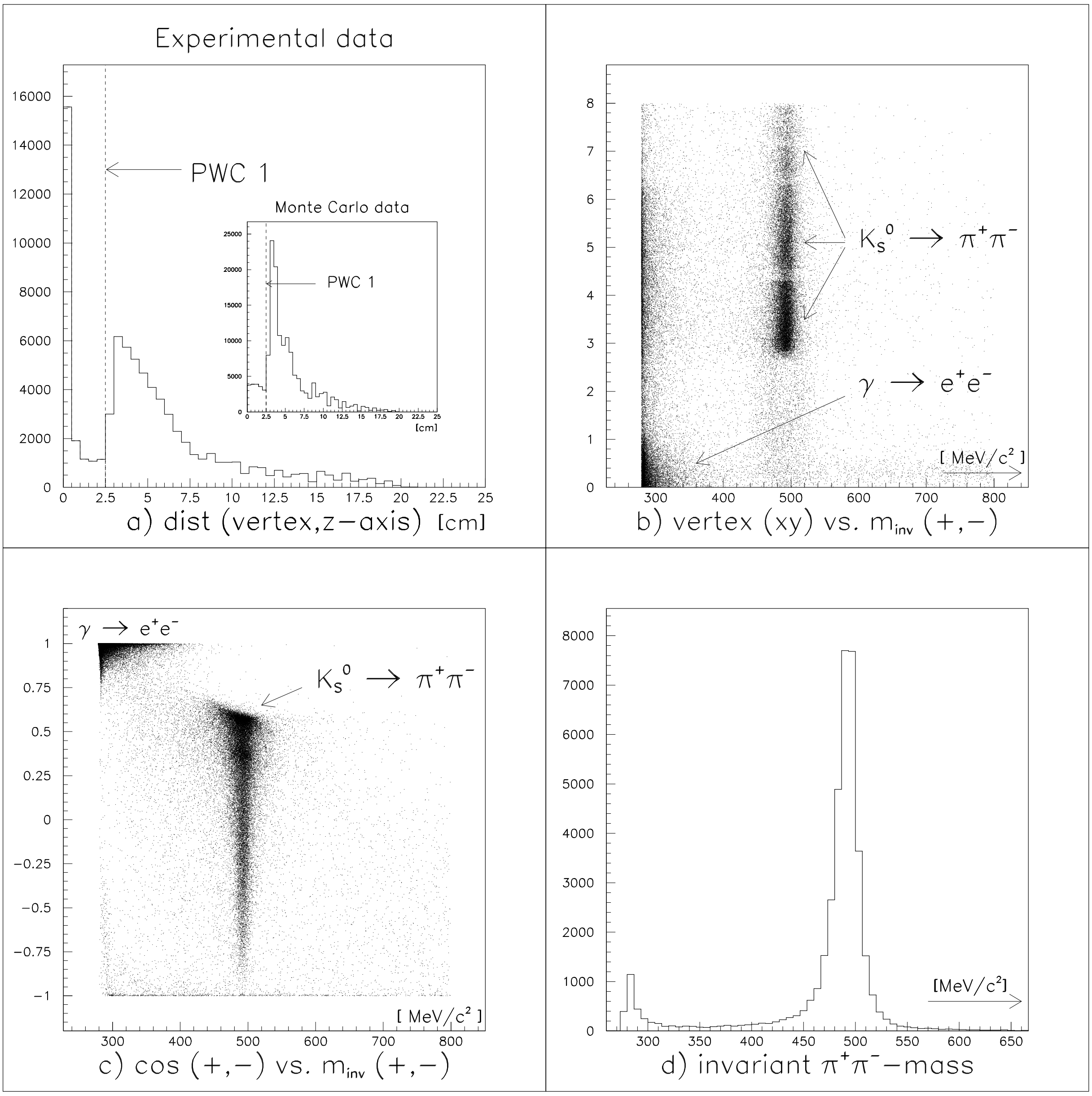

Figure 1.3: *For many real events the charged vertex was found by the reconstruction at the origin (**a**) but this is not the case for the Monte Carlo data of the final state $K_S^0 K_S^0 \pi^0$. From **b** and **c** one can conclude that these events are mainly due to γ-conversions into e^+e^-. **d** shows the invariant π^+ π^- -mass spectrum before the kinematic fit.*

Statistics of the preselection

1) $p\overline{p} \longrightarrow K_S^0(\pi^+\pi^-)\ K_S^0(\pi^0\pi^0)\ \pi^0/\eta$

	Experiment	Monte Carlo	
		$K_S^0K_S^0\pi^0$	$K_S^0K_S^0\eta$
Events (MC : $r_{xy}(K_S^0 \rightarrow \pi^+\ \pi^-\ ) > 2.5\ cm$) (without bias corresponding to)*	1 665 132	835 572 ($\rightsquigarrow$ 2 851 782)	171 701 ($\rightsquigarrow$ 964 612)
trigger conditions ok.	1 605 571	342 913	60 054
2 charged tracks	857 666	290 059	51 412
vertex : $r_{xy} > 2.5\ cm\ \wedge\ r_z < 10\ cm$	579 101	258 695	47 232
charge sum = 0	536 516	251 295	46 168
energy sum = 1.55 - 2.20 GeV	292 069	242 781	44 263
$cos(\vec{P}_{\pi^+},\vec{P}_{\pi^-}) < 0.75$	145 545	242 007	44 184
no PED in crystal type 13	129 278	211 344	37 533
6 PEDs	30 956	94 191	16 072
7 PEDs	14 264	28 202	5 895

2) $p\overline{p} \longrightarrow K_S^0(\pi^+\pi^-)\ K_S^0(\pi^+\pi^-)\ \pi^0/\eta$

	Experiment	Monte Carlo	
		$K_S^0K_S^0\pi^0$	$K_S^0K_S^0\eta$
Events (MC : $r_{xy}(K_S^0 \longrightarrow \pi^+\ \pi^-\ ) > 2.5\ cm$) (without bias corresponding to)*	1 665 132	319 890 ($\rightsquigarrow$ 3 477 065)	74 264 ($\rightsquigarrow$ 2 395 613)
trigger conditions ok.	1 605 571	184 645	31 695
4 charged tracks	286 310	115 945	20 141
2 vertices : $r_{xy} > 2.5\ cm\ \wedge\ r_z < 10\ cm$	32 371	55 203	9 811
energy sum = 1.55 - 2.20 GeV	24 081	51 953	9 317
$cos(\vec{P}_{\pi^+},\vec{P}_{\pi^-}) < 0.75$	21 875	51 676	9 259
no PED in crystal type 13	20 646	48 284	8 659
2 PEDs	8 457	21 468	3 951
3 PEDs	3 193	12 249	1 972

Table 1.2: **Monte Carlo events with the xy-component of the secondary vertex* $K_S^0 \rightarrow \pi^+\ \pi^-$ *being less than 2.5 cm have not been fully generated since the efficiency of the inner PWC 1 is close to 100 %. The reliability of this step will be discussed in chap 1.5.*

1.4 The kinematic fit

1.4.1 Kinematic fit with one neutral K^0_S-decay

For events of type (1.1) the kinematic fit is done with respect to the following hypotheses :

(1a) $p\overline{p} \rightarrow K^0_S\ \pi^+\ \pi^-\ \gamma\gamma\ \ (K^0_S \rightarrow \pi^0\ \pi^0\ )$

(1b) $p\overline{p} \rightarrow K^0_S\ K^0_S\ \gamma\gamma$

(1c) $p\overline{p} \rightarrow K^0_S\ K^0_S\ \pi^0\ (\eta)$

In case of 7-PED events the first hypothesis is applied seven times, each time one of the PEDs is dropped. This procedure acts as an additional method to identify splitoffs.

The unknown vertex of the decay $K^0_S \rightarrow \pi^0\ \pi^0$ makes it not advisable to apply a normal 4C-fit at the first step as it is usually done in other channels, since the shifted vertex leads to a wrong measurement of the three-momenta of the gammas. They have to be corrected in the first step of the kinematic fit, otherwise too many events would get lost (and a systematic effect would be introduced into the analysis !).

An option to fit the vertex coordinates of $K^0_S \rightarrow \pi^0\ \pi^0$ is implemented in the CBKFIT ('CASE 8') but so far the fit systematically rejects events where this vertex is close to the origin [15]. This can be shown by the investigation of Monte Carlo data where the 'true' (= generated) vertex is known.

For all Monte Carlo events with $CL > 1\%$ according to hypothesis (1a) the 'true' vertex distribution (fig. 1.4b) is different from the one of all generated Monte Carlo data (fig. 1.4a). If r_e is the value where the distribution has reached 1/e of the value at $r = 0$ (r being the distance between the decay vertex and the z-axis) then the value for data accepted by the fit ($r_e^{C8} = 2.8\ cm$) is larger than for the complete data sample ($r_e^{all} = 1.8\ cm$).

It is suggestive to take now all the events rejected by the first hypothesis and to do the same kinematic fit again but setting the vertex of the neutral K^0_S-decay in the fit to (0,0,0) ('CASE 1' in CBKFIT). Fig. 1.4c shows the 'true' vertex distribution of those events with $CL > 1\%$ according to hypothesis (1a) and for them one gets $r_e^{C1} = 1.2\ cm$ (which is now of course much smaller than r_e^{all}). However, if the events in fig. 1.4b and 1.4c are added (fig. 1.4d) then the vertex distribution of the generated events and of all events accepted by this fit procedure ($r_e^{C8+C1} = 1.8\ cm\ =\ r_e^{all}$) agree very well. Therefore it can be concluded that this method to fit events with a neutral K^0_S-decay is very reasonable and successful though it looks somehow artificial at a first glance.

After the first hypothesis the vertex of the neutral K^0_S-decay is fixed and also the gammas which belong to it. Now hypothesis (1b) is applied and for all events with $CL > 1\%$ according to this hypothesis the invariant mass spectrum of the two single gammas shows clear peaks at the π^0- and at the η-mass (fig. 1.8).

Finally events are fitted to hypothesis (1c) requiring the confidence level being larger than 5%. Results are shown in tab. 1.3.

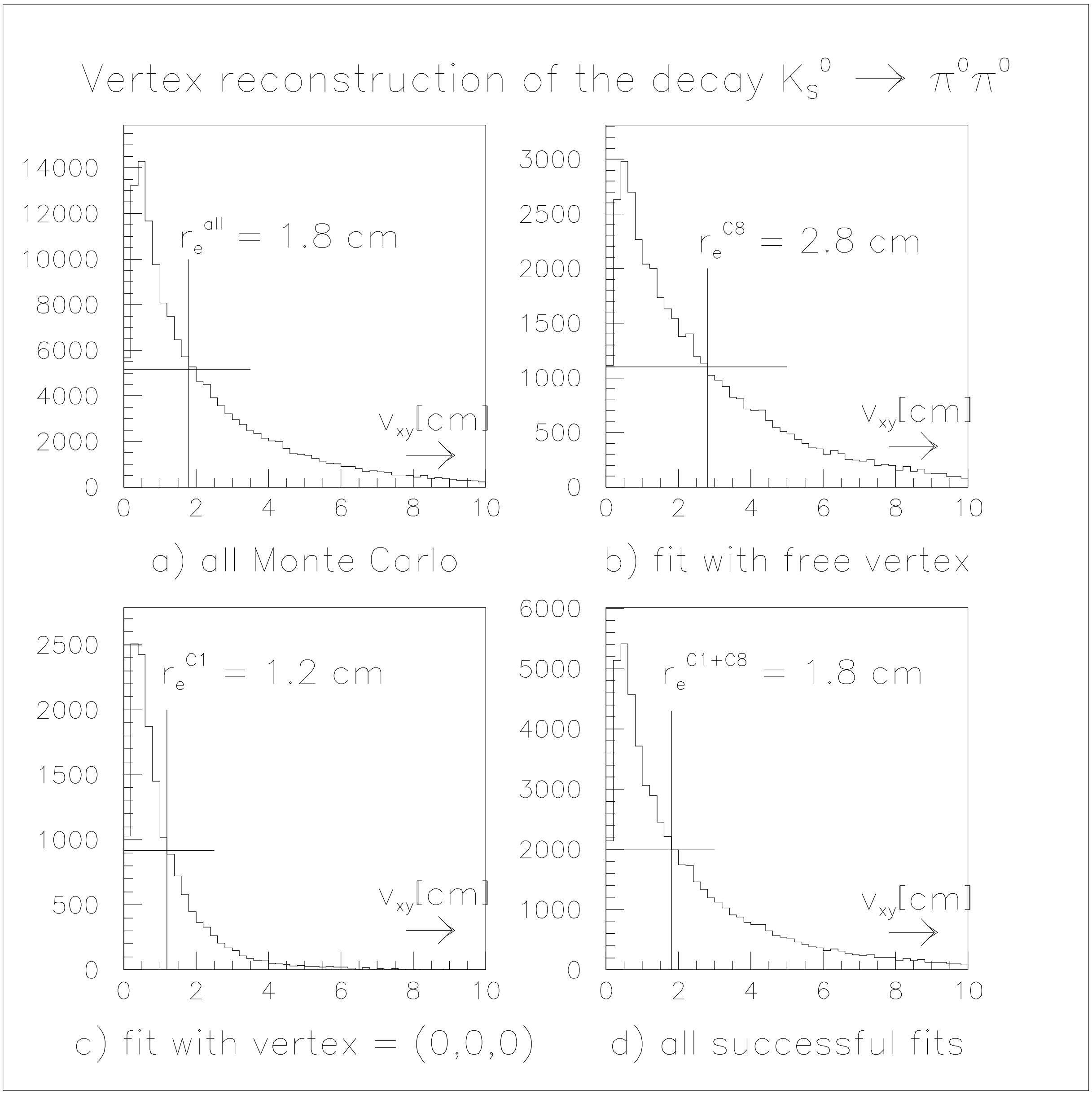

Figure 1.4: *Vertex reconstruction of the decay* $K_S^0 \rightarrow \pi^0\ \pi^0$.
a *: 'true' vertex distribution of the complete Monte Carlo data sample.*
b *: 'true' vertex for all events with* $CL > 1\%$ *with respect to hypothesis (1a).*
c *: 'true' vertex for all events with* $CL > 1\%$ *with respect to hypothesis (1a) if the vertex coordinates are set to (0,0,0) in the kinematic fit and* CL *was* $< 1\%$ *for the free vertex fit.*
d *: 'true' vertex for all events in* **b and c**

		Experimental data		Monte Carlo $K_S^0K_S^0\pi^0$		Monte Carlo $K_S^0K_S^0\eta$	
Hypothesis	CL	vertex free	vertex (0,0,0)	vertex free	vertex (0,0,0)	vertex free	vertex (0,0,0)
before CBKFIT	-	45 220		122 393		21967	
$K_S^0\pi^+\pi^-\gamma\gamma$ $K_S^0\rightarrow\pi^0\pi^0$	>0.01	10 978	4 589	53 666	20 213	8046	2774
$K_S^0K_S^0\gamma\gamma$ $K_S^0\rightarrow\pi^+\pi^-$ $K_S^0\rightarrow\pi^0\pi^0$	>0.01	9 094	3 370	39 959	13 410	5809	1736
$K_S^0K_S^0\pi^0$ $K_S^0K_S^0\eta$	>0.05 <0.01	7 491	2 555	33 492	11 296	11	6
$K_S^0K_S^0\eta$ $K_S^0K_S^0\pi^0$	>0.05 <0.01	211	159	3	1	3 515	2 951

Table 1.3: *Statistics of the kinematic fit with one neutral K_S^0-decay.*

Error scaling and adjustment of the pulls

Due to remaining systematic uncertainties caused mainly by the unknown neutral K^0_S-vertex and due to background from other channels the confidence level distribution (fig. 1.7) is not completely flat with a sharp peak at zero as it would be in the most idealistic case. It was pointed out by R. McCrady [16] that it could be advantageous in that case to adjust the pulls according to the following procedure.

For each kinematic variable the pulls are plotted for different CL-cuts and the widths of the pulls are determined in dependence of the CL-cut by a fit with a Gaussian. It turns out that the width is decreasing linearly with increasing confidence level cut, so the correction of the errors should be done in that way that the extrapolation to a CL-cut of zero leads to $\sigma(pulls) = 1$.

As an example the pulls of $tg(\lambda)$ are shown in fig. 1.5 for different CL-cuts and the fitted mean values and widths are given.

Fig. 1.6 shows the result of this procedure for experimental data after scaling the errors. Different scaling factors for the elements of the covariant error matrix have been used for the kinematic fit with and without fitting the vertex of $K^0_S \rightarrow \pi^0\ \pi^0$ and for fitting experimental and Monte Carlo data (tab. 1.4). In order to center the pulls exactly around zero a constant value has been added to $tg(\lambda)$ and $1/P_{xy}$ has been multiplied by another scaling factor.

		θ	$\sqrt{E}$	φ	$1/P_{xy}$	$tg(\lambda)$	ψ	$*1/Pxy$	$+tg(\lambda)$
Experimental	CASE 8	1.00	0.95	1.10	1.10	1.15	1.25	0.992	-0.012
data	CASE 1	1.00	1.20	1.00	1.10	1.15	1.25	0.980	-0.017
Monte	CASE 8	1.10	1.00	1.20	1.25	1.20	1.25	1.000	-0.005
Carlo	CASE 1	1.05	1.00	1.10	1.05	1.22	1.15	0.990	0.000

Table 1.4: **columns 1-6 :** *The values of the covariant error matrix used in CBKFIT are multiplied by the scaling factors in this tabular in order to adjust the pulls.*
column 7 : *The kinematic variable* $1/P_{xy}$ *used in CBKFIT is multiplied by this factor in order to center the pull of* $1/P_{xy}$ *around zero.*
column 8 : *Added to the kinematic variable* $tg(\lambda)$ *in order to center the pull of* $tg(\lambda)$ *around zero.*

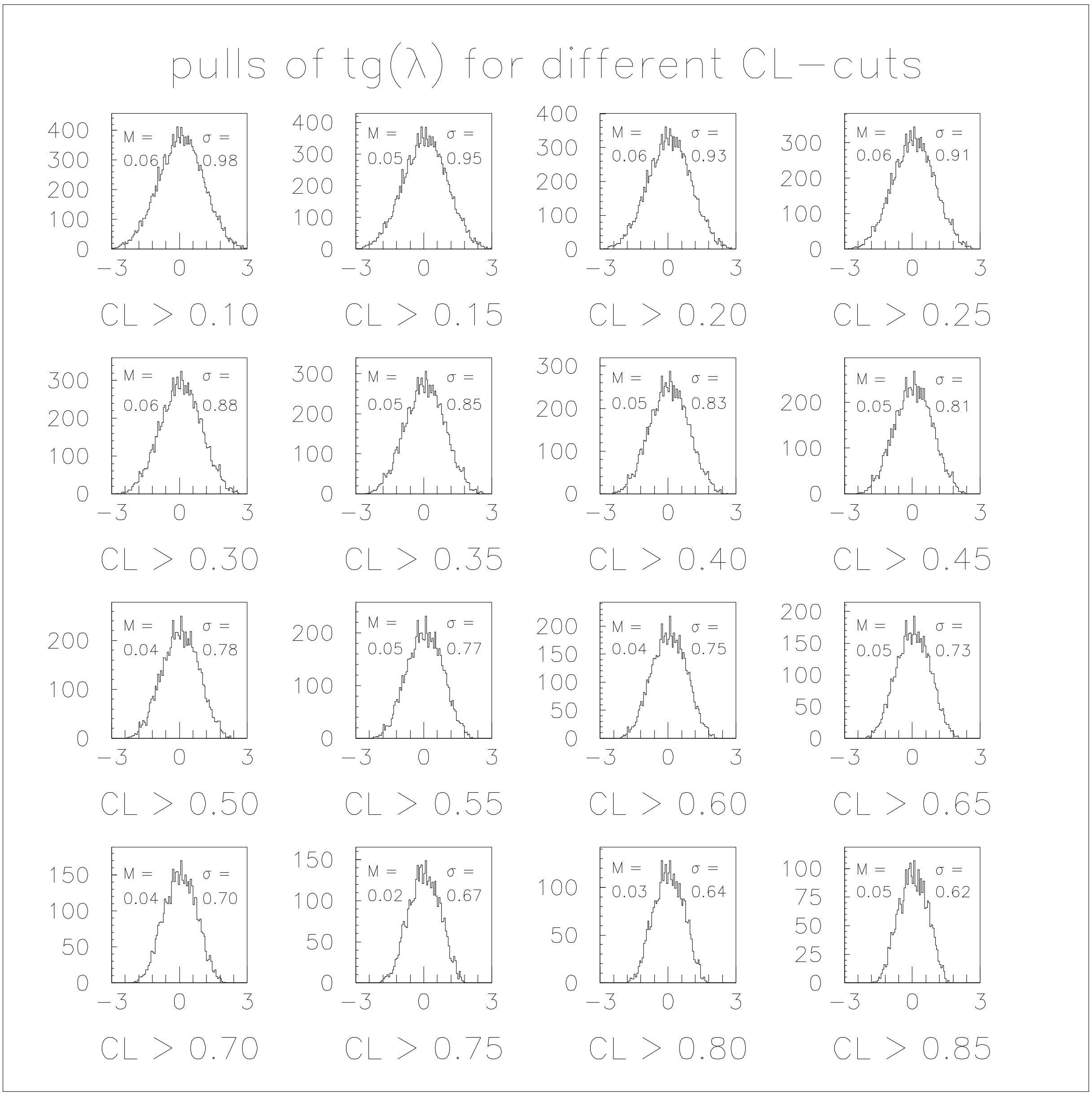

Figure 1.5: *As an example for the way how the pulls have been adjusted the pulls for* $tg(\lambda)$ *are plotted for different CL-cuts. For each of these cuts the respective pull is fitted with a Gaussian. The values* M *and* σ *are the mean and the width obtained by the fit.*

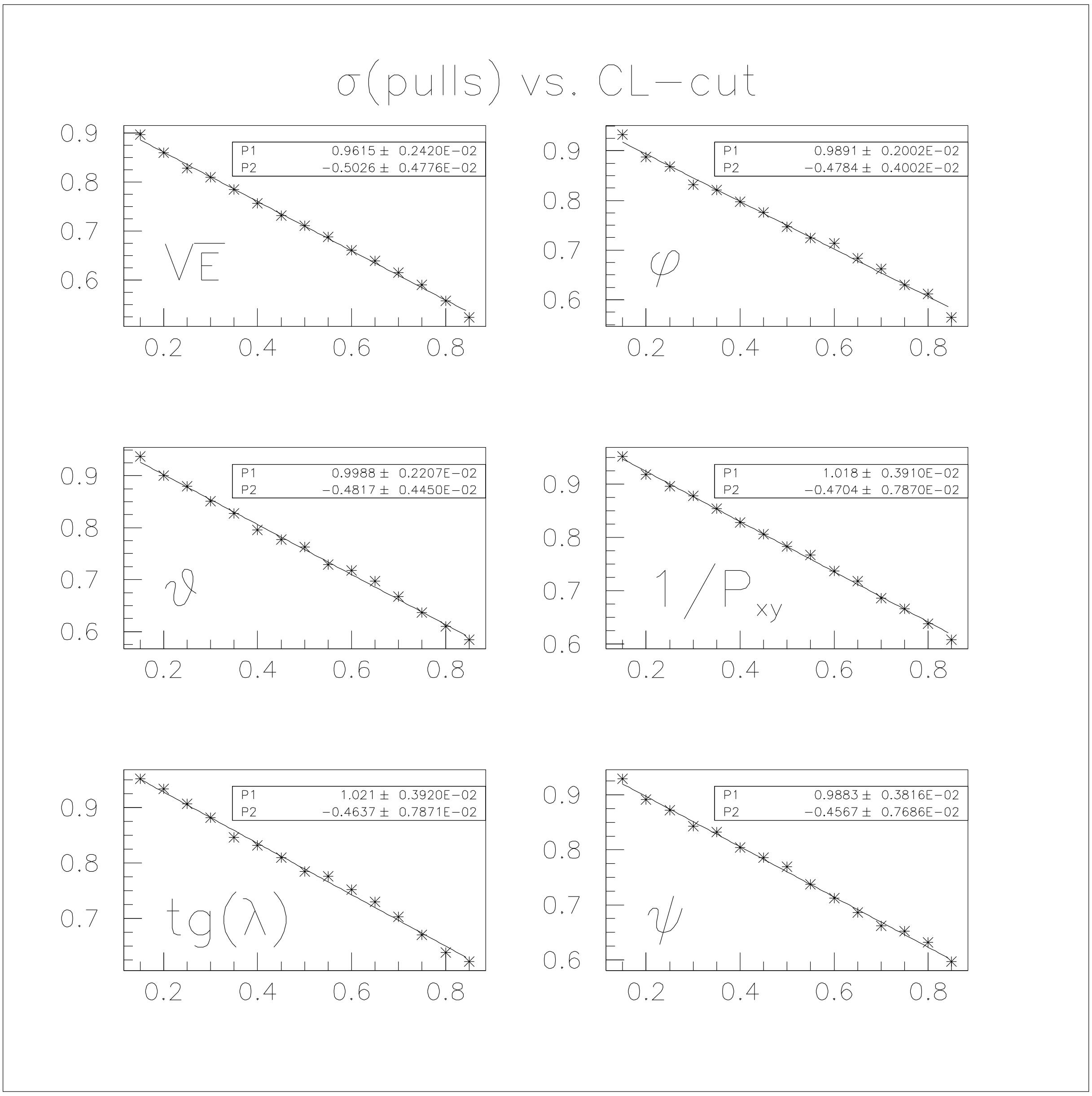

Figure 1.6: *The errors have been adjusted in that way that the width of each pulls would become 1 for a hypothetical CL-cut at 0. P1 and P2 are the parameters obtained by fitting the values with a linear function.*

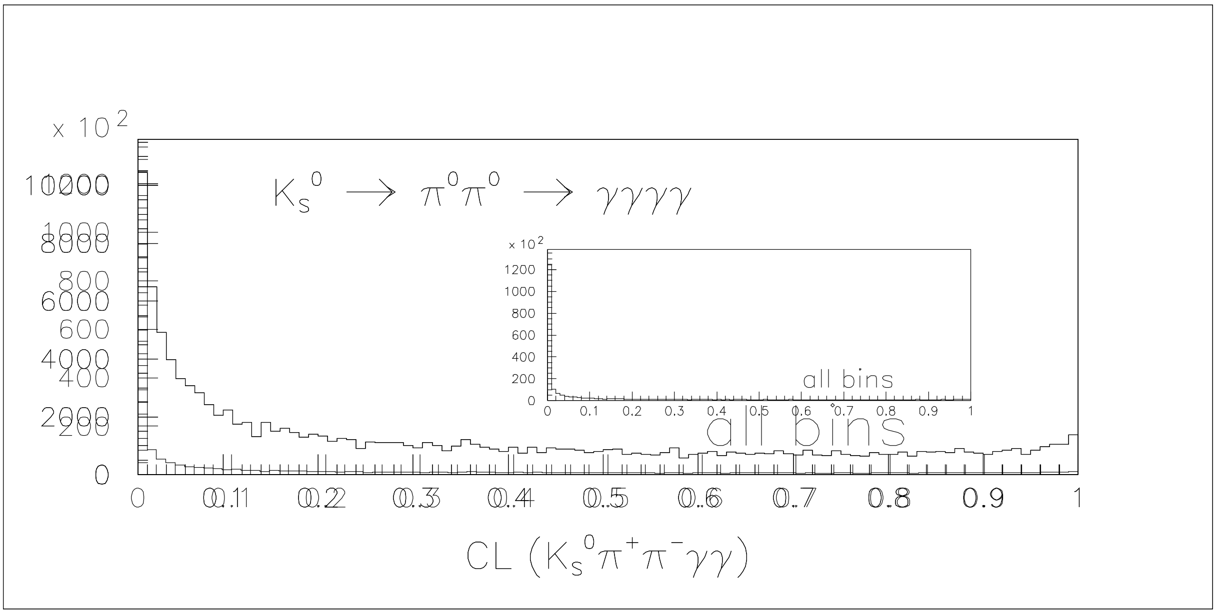

Figure 1.7: *The confidence level distribution for the hypothesis* $p\bar{p} \rightarrow K_S^0\ \pi^+\ \pi^-\ \gamma\gamma$ *with* $K_S^0 \rightarrow \pi^0\ \pi^0$ *. The small histogram shows all bins, the first bin is skipped for the large histogram.*

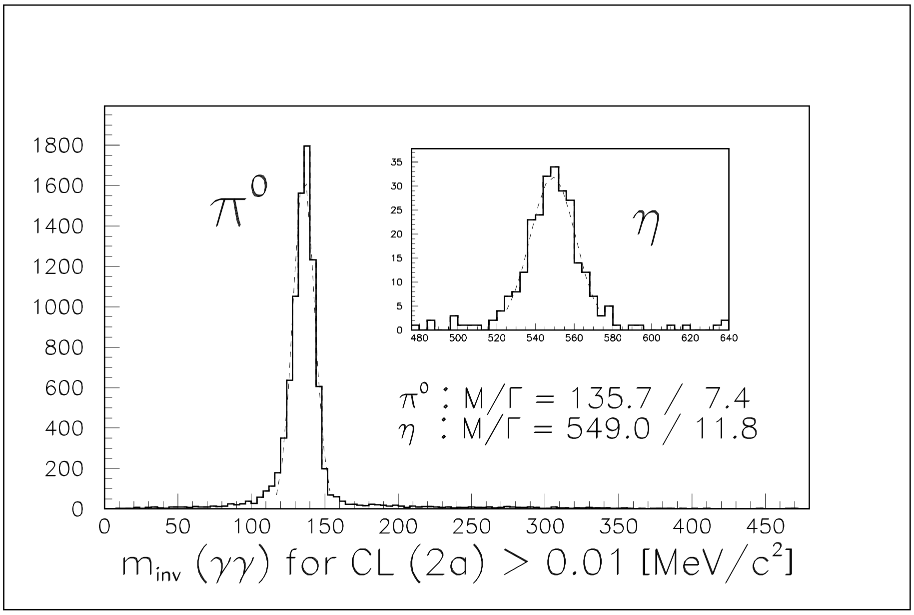

Figure 1.8: *Before the kinematic fit with respect to the final hypothesis is done the invariant* $\gamma\gamma$*-mass shows clear signals at the* π^0*- and at the* η*-mass. Both signals are almost free of background and the masses and widths obtained by a fit of the peaks with a Gaussian agree very well with the values of [1].*

Quality of the K_S^0-signals

From fig. 1.9a and b the mass and the width of the K_S^0 can be determined by a Gaussian for the experimental and for the simulated data. The widths correspond to the experimental resolution.

Before adjusting the pulls the mass of the experimental data spectrum is shifted to lower values. After the adjustment it agrees quite good with [1] but a slight asymmetry remains. This indicates a slight systematic error in the experimental measurement, maybe due to the fact that the beam was steered a little bit below the beam axis in the 10/93 run because of problems with gas bubbles. The effect, however, is very small and will not cause any problem for the further data analysis.

The measurement of the K_S^0 via its neutral decay mode definitely improved by determing the vertex coordinates with the kinematic fit though it cannot compete with the measurement via its charged decay mode.

The K_S^0-mass acts as a constraint in the kinematic fit, but the resolution of its vertex coordinates and of each component of its four-vector can be determined from Monte Carlo data. The difference between measured and 'true' value is plotted and then fitted with a Gaussian (fig 1.10).

It turns out that the measurement of the z-coordinate of the secondary vertex of the neutral K_S^0-decay (fig. 1.10d and f) is almost as good as for the charged decay (fig. 1.10b), in the xy-plane the result is definitely worse (fig. 1.10a,c and e).

Tab. 1.5 summarizes the resolution of the vertex and four-vector components, the resolution of the Dalitz plot variables will be shown in chap. 1.6.

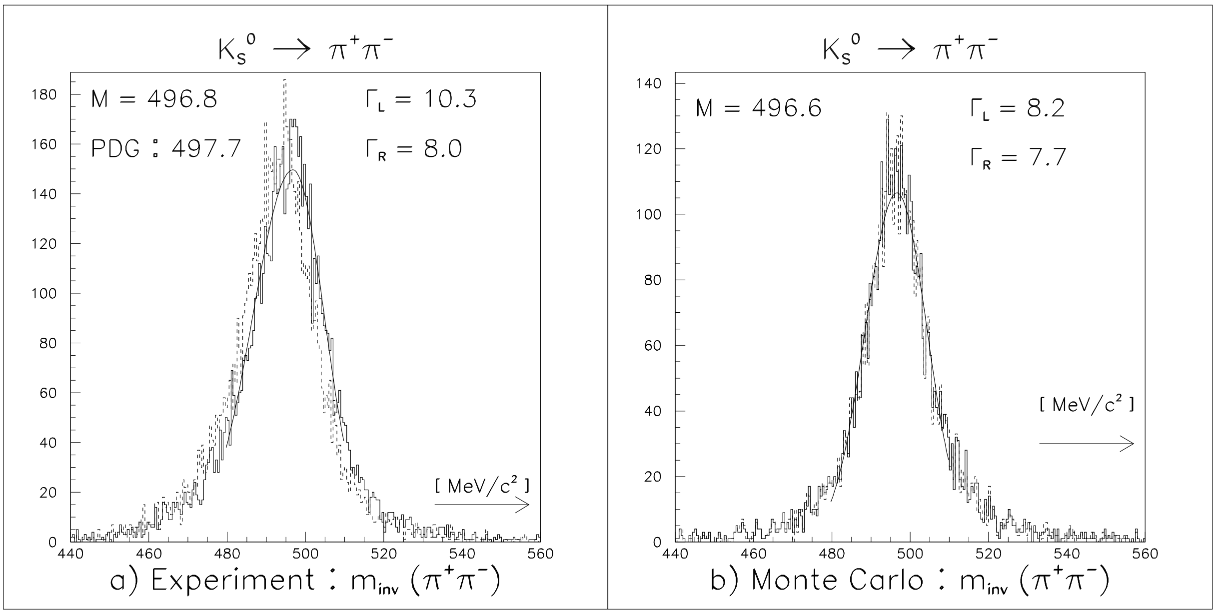

Figure 1.9: *After adjusting the pulls (solid line) the peak of the K_S^0 in the π^+ π^- -invariant mass spectra agrees almost perfectly well with the value of [1] ($M(K_S^0) = 497.67 MeV/c^2$) for both experimental* **(a)** *and Monte Carlo data* **(b)**. *For the for experimental data it was slightly shifted to lower mass before the adjustment (dotted lines).*

Differences between generated and reconstructed values	$K_S^0 \to \pi^+ \pi^-$		$K_S^0 \to \pi^0 \pi^0$			
			CASE 8		CASE 1	
	Mean	Width	Mean	Width	Mean	Width
Vertex : xy-plane [cm]	0.60	0.25	0.60	1.28	-	1.12
Vertex : z-component [cm]	-0.11	0.45	0.17	0.48	-0.12	0.45
Momentum [MeV/c]	0.83	15.42	1.07	6.83	-2.96	8.15
Energy [MeV]	2.65	14.69	1.23	8.82	-1.84	8.15

Table 1.5: *The reconstruction quality of the neutral decaying K_S^0. The four-vectors obtained from the kinematic fit agree very well with their 'true' values though the reconstruction of the vertex coordinates in the xy-plane is not yet perfect. For the charged decay of the K_S^0 the four-vectors are taken from the LOCATER bank.*

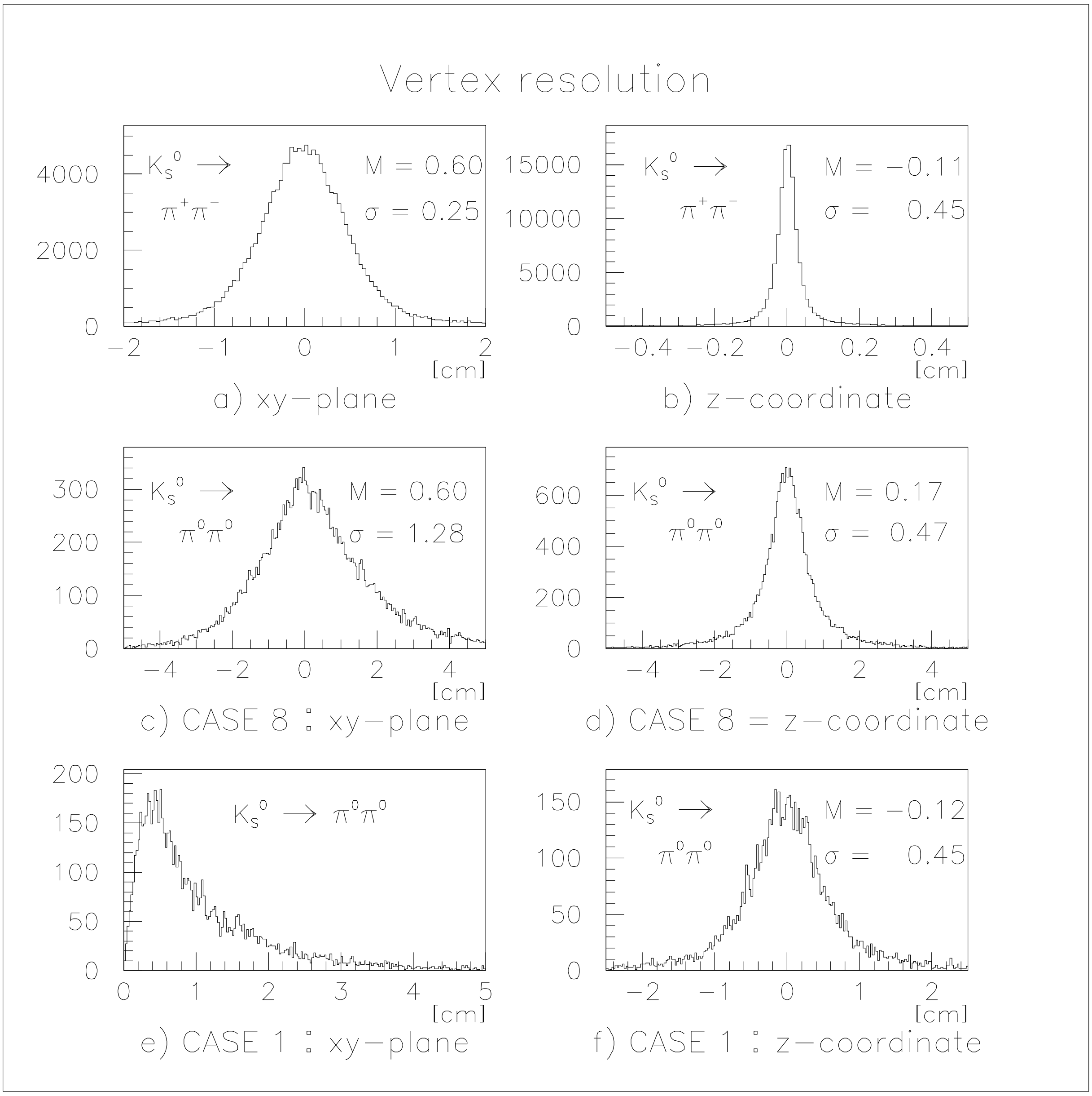

Figure 1.10: *The vertex resolution is defined as the difference between the 'true', i.e. generated, values of the Monte Carlo simulation and the values obtained by the kinematic fit. The resolution of the z-coordinate is equally good for charged and neutral* K_S^0*-decays, in the xy-plane the resolution is definitely better in case of charged* K_S^0*-decays.*

1.4.2 Kinematic fit with two charged K_S^0-decays

Since two secondary vertices have already been found in each event of this data subset by the reconstruction and all tracks are assigned to a vertex, these informations should be imposed on the kinematic fit. Therefore only the two following hypotheses are applied for these data :

(2a) $K_S^0\ K_S^0\ \gamma\gamma$

(2b) $K_S^0\ K_S^0\ \pi^0(\eta)$

The same method as in chap. 1.4.1 has been applied for adjusting the pulls (fig. 1.11) scaling factors are given in tab. 1.6). Since there are no such uncertainties in these events like the unknown vertex of a neutral K_S^0-decay, the confidence level distribution (fig. 1.12) does not show such a smooth decrease between 0.01 and 0.2 as in fig. 1.7.

	θ	$\sqrt{E}$	φ	$1/P_{xy}$	$tg(\lambda)$	ψ	$*1/Pxy$	$+tg(\lambda)$
Experiment	1.12	1.02	0.97	1.07	1.17	1.25	0.990	0.000
Monte Carlo	1.50	0.91	1.19	1.07	0.90	1.09	1.000	-0.005

Table 1.6: *Scaling factors for the kinematic fit with two charged K_S^0-decays. The meaning of all values is identical to those of tab. 1.4*

Tab 1.7 summarizes the results of this kinematic fit and the applied CL-cuts.

Hypothesis	CL	Experiment	Simulation	
			$K_S^0K_S^0\pi^0$	$K_S^0K_S^0\eta$
before CBKFIT	-	11 650	33 717	5 923
$K_S^0K_S^0\gamma\gamma$ $K_S^0\to\pi^+\pi^-$ $K_S^0\to\pi^+\pi^-$	>0.01	6 564	19 941	3 421
$K_S^0K_S^0\pi^0$ $K_S^0K_S^0\eta$	>0.05 <0.01	5 782	18 388	0
$K_S^0K_S^0\eta$ $K_S^0K_S^0\pi^0$	>0.05 <0.01	141	0	3 303

Table 1.7: *Statistics of the kinematic fit with two charged K_S^0-decays.*

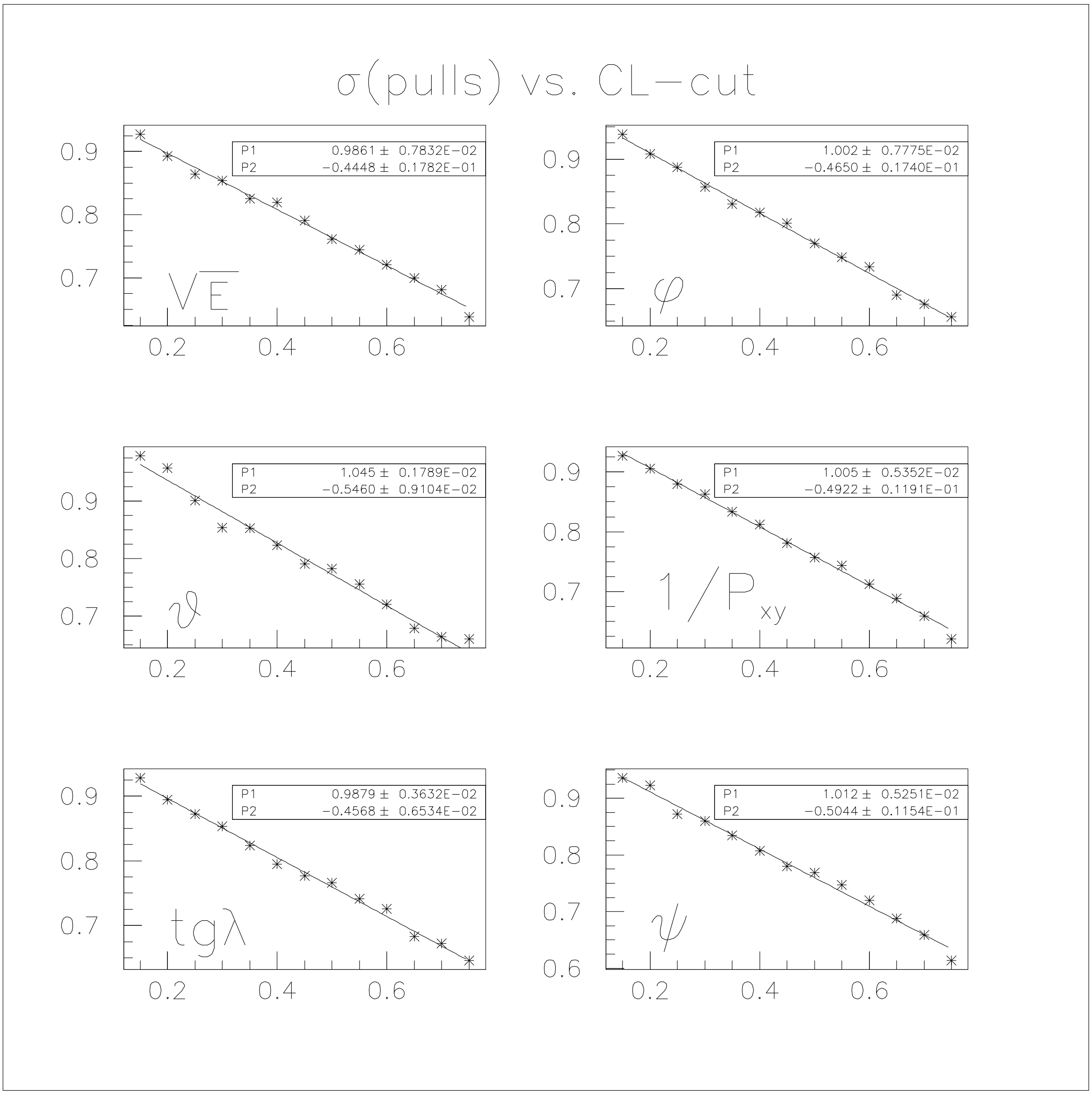

Figure 1.11: *The errors have been adjusted in the same way as for events with one neutral K_S^0-decay. This figure is equivalent to fig. 1.6*

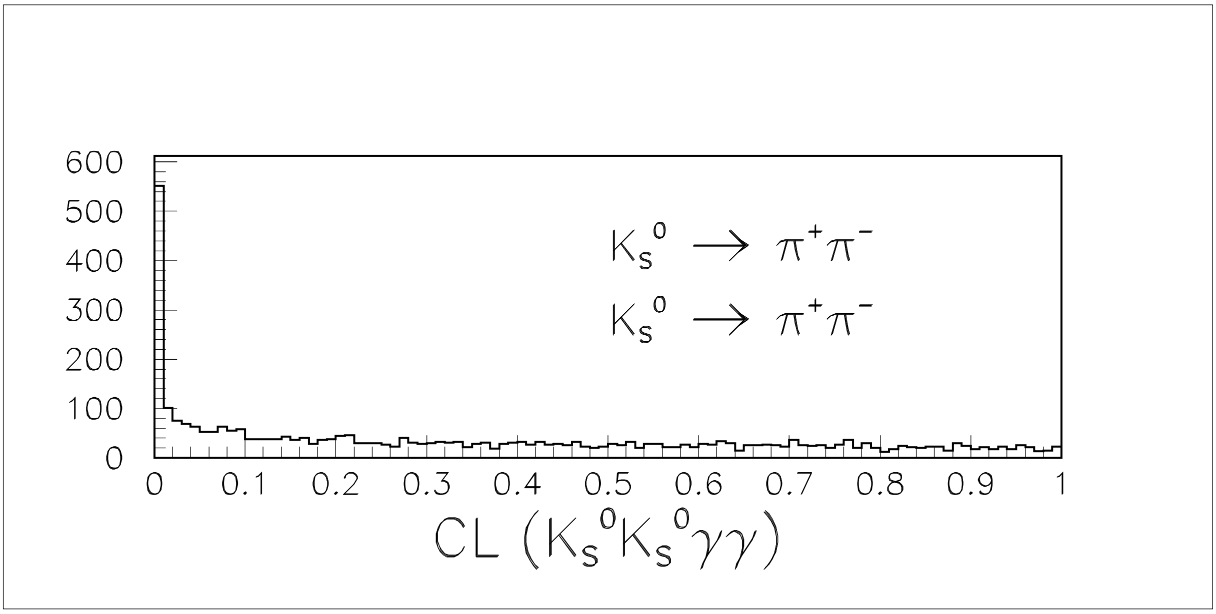

Figure 1.12: *The CL-distribution of events with two charged K_S^0-decays. Events with $CL < 1\%$ will be rejected.*

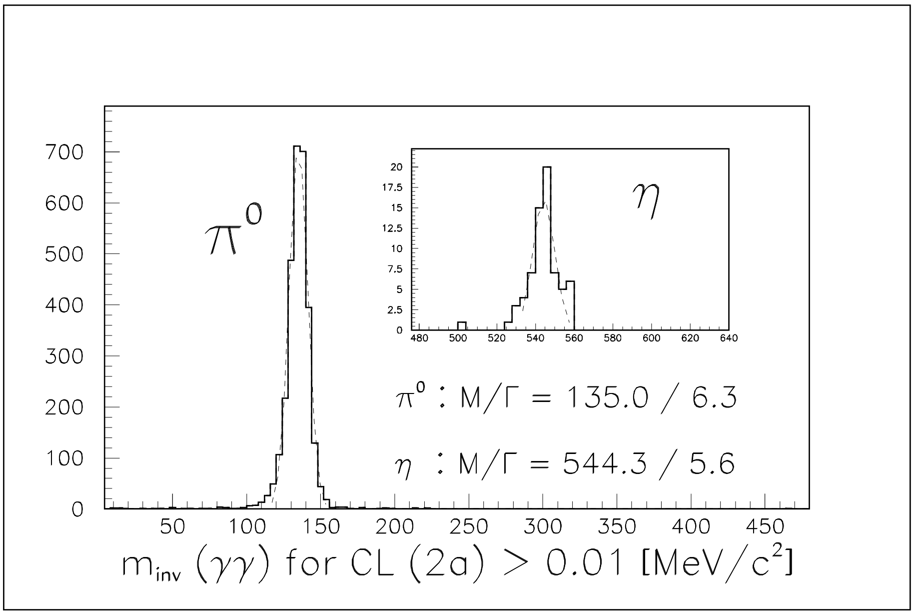

Figure 1.13: *The masses and widths of the peaks in the $\gamma\gamma$-spectrum before the last step of the kinematic fit agree very well with the nominal values of π^0 and η.*

1.5 Background in the Dalitz plot $K_S^0 K_S^0 \pi^0$

The remaining background in the Dalitz plot of the final state $K_S^0 K_S^0 \pi^0$ can be estimated in two different ways.

Invariant mass spectra

The first way to estimate the background is to look at the invariant mass spectra. The $\pi^+ \pi^-$ mass spectrum before the kinematic fit (fig. 1.14a) shows that triggering on $K_S^0 \rightarrow \pi^+ \pi^-$ and the reconstruction of the charged tracks and secondary vertices works very well, so that almost all background in the $K_S^0 K_S^0 \pi^0$ final states must come from other $K_S^0 K_S^0$-channels (events from $K_S^0 K_L^0$-channels have been excluded by the cut on the total energy).

The $\gamma\gamma$-mass spectrum for all events with $CL > 1\%$ with respect to hypothesis (1b) or (2a) is shown in fig. 1.14b. There is now - before the final hypothesis - almost no background anymore below the π^0-peak. From fig. 1.14b one can estimate that the amount of background events in the Dalitz plot will be less than 3%.

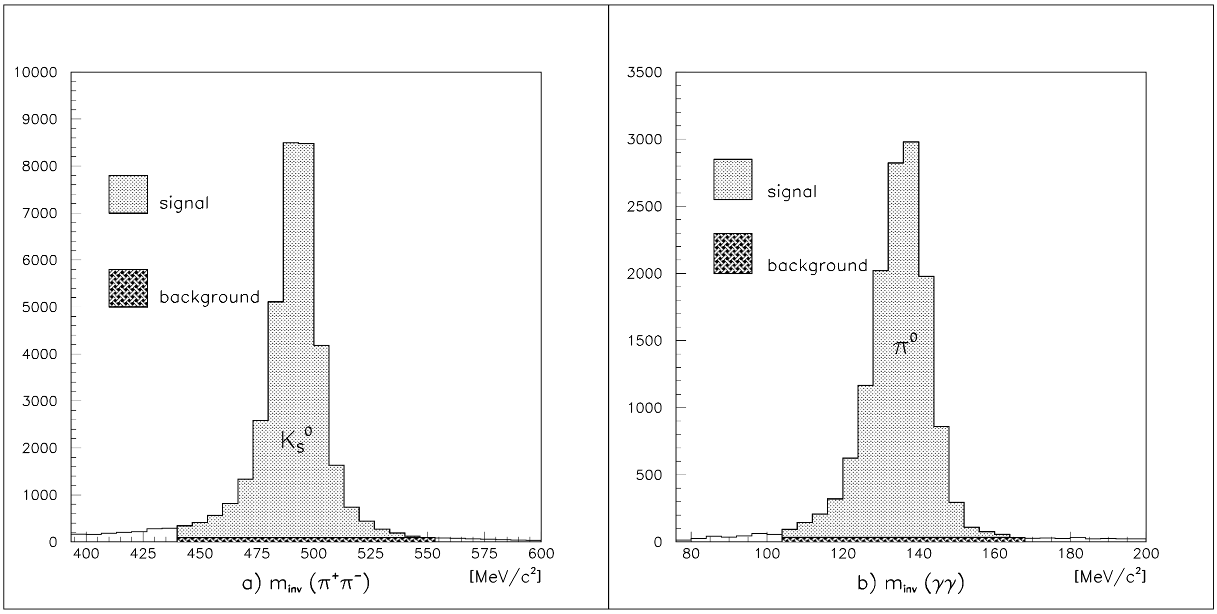

Figure 1.14: *The K_S^0-signal in the invariant $\pi^+\pi^-$-signal spectrum and the π^0-mass in the invariant $\gamma\gamma$-mass spectrum. From the latter one can estimate the total background in the Dalitz plot being less than at least 3%.*

Simulation of possible background channels

Another way to estimate the background is to generate events of the possible background channels and to analyze them in the same way as the data. Taking into account the absolute branching ratios of these channels and the values of tab. 1.1 the amount of background events in the Dalitz plot can be estimated.

In tab. 1.8 the investigated background channels and their contribution is shown.

background channel ($K^0_SK^0_SX$)	$BR(p\bar{p} \longrightarrow K^0_SK^0_SX)$ $[10^{-4}]$	fully generated	events in Monte Carlo Dalitz plot	events in experimental Dalitz plot
$K^0_SK^0_S\pi^0$ $r_{xy} < 2.5$ cm	7.5 ± 0.3	150 000	30	90 ± 18
$K^0_SK^0_S$	< 0.05	45 933	9	< 4
$K^0_SK^0_S\eta(\eta\to\gamma\gamma)$	0.97 ± 0.16	171 701	4	0.3
$K^0_SK^0_S\omega(\omega\to\pi^0\gamma)$	0.92 ± 0.14	26 897	3	0.6
$K^0_SK^0_S\pi^0\ \pi^0$	< 0.09	39 706	2	< 6

Table 1.8: *Different possible background channels of the final state $K^0_SK^0_S\pi^0$ have been generated and their contribution in the Dalitz plot has been determined. Some of these channels can only feed through if PEDs are lost or misidentified as splitoffs or if splitoffs are misidentified as PEDs.*

Due to the excellent trigger performance any background can only come from other $K^0_SK^0_S$-channels. The simulation however shows that none of the possible channels will in fact contribute significantly under the assumption that all physical processes, including the hadronic interaction of the charged pions in the barrel, are well understood. The only background comes from $K^0_SK^0_S\pi^0$-events with a vertex closer than 2.5 cm from the beam axis. These events have not been fully generated by Monte Carlo since the effect is small ($< 1\%$) and a large amount of computing time was saved (infact it is not real background but a slight uncertainty in the Monte Carlo simulation).

From fig. 1.14 it was estimated that the background is less than at least 3%. This, however, was the most pessimistic conclusion drawn from the invariant $\gamma\gamma$-mass spectrum.

Hence it is justified to claim that the physical background from other channels is negligible in the Dalitz plot of the final state $K^0_SK^0_S\pi^0$.

1.6 The Dalitz plots of $p\bar{p} \rightarrow K^0_S K^0_S \pi^0$ and $p\bar{p} \rightarrow K^0_S K^0_S \eta$

The resolution of the Dalitz plot variables (fig. 1.15) and the very low background (chap. 1.5) gives much confidence in the data set that will be used for the partial wave analysis.

The major problem is the bias introduced by the trigger which leads to a very low acceptance for charged decaying K^0_S with low momentum. In the Dalitz plots (fig. 1.16a and b) the number of entries in the respective area is very low and the two projections on the $m^2(K\pi)$-axis (fig. 1.16c) in the case of one charged and one neutral K^0_S-decay differ clearly from each other.

If one likes to bin the data one should choose the bin size according to the resolution of the Dalitz plot variables. This resolution is defined as the difference between the values from the kinematic fit and the generated values (Monte Carlo data). From fig. 1.15 one can conclude that the bin size should be larger than at least 0.05 GeV^2/c^4.

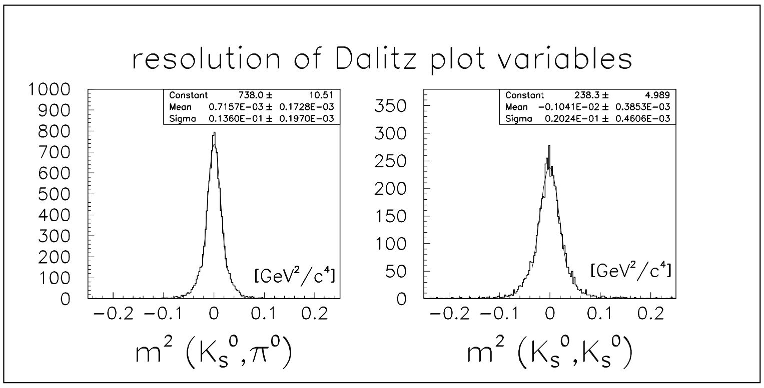

Figure 1.15: *The resolution of the Dalitz plot variables is defined as the difference between their values obtained by the kinematic fit and their 'true' (= Monte Carlo generated) values.*

Number of events in the Dalitz plots

final state	$K^0_S K^0_S \pi^0$		$K^0_S K^0_S \eta$	
decay mode	$K^0_S \longrightarrow \pi^+ \pi^-$ $K^0_S \longrightarrow \pi^0 \pi^0$	$K^0_S \longrightarrow \pi^+ \pi^-$ $K^0_S \longrightarrow \pi^+ \pi^-$	$K^0_S \longrightarrow \pi^+ \pi^-$ $K^0_S \longrightarrow \pi^0 \pi^0$	$K^0_S \longrightarrow \pi^+ \pi^-$ $K^0_S \longrightarrow \pi^+ \pi^-$
Experimental data	10 046	5 782	370	141
Monte Carlo data	44 788	18 388	5 346	3 303

Table 1.9: *Number of events in the Dalitz plots of the final states $K^0_S K^0_S \pi^0$ and $K^0_S K^0_S \eta$ for experimental as for Monte Carlo data.*

Dalitz plots and projections

$$\boxed{p\bar{p} \rightarrow K^0_S\, K^0_S\, \pi^0}$$

$$K^0_S \rightarrow \pi^0\, \pi^0 \qquad\qquad K^0_S \rightarrow \pi^+\, \pi^-$$

$$K^0_S \rightarrow \pi^+\, \pi^- \qquad\qquad K^0_S \rightarrow \pi^+\, \pi^-$$

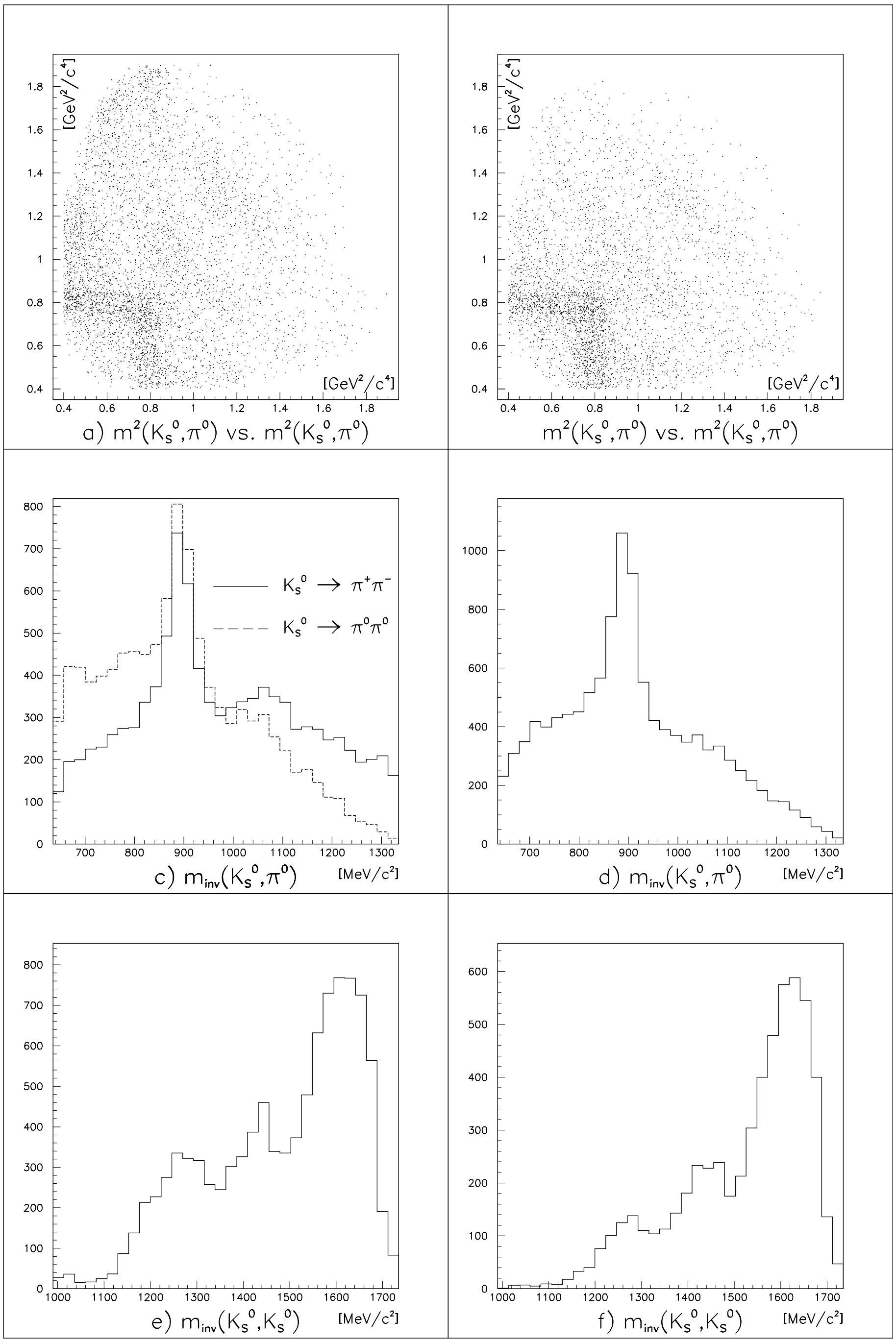

Figure 1.16: *The Dalitz plots for the final state $K^0_S K^0_S \pi^0$ for the data subsets with one (left column) and two (right column) charged K^0_S-decays and their projections.*

Dalitz plots and projections

$$\boxed{p\overline{p} \to K^0_S\, K^0_S\, \eta}$$

$K^0_S \to \pi^0\, \pi^0$

$K^0_S \to \pi^+\, \pi^-$

$K^0_S \to \pi^+\, \pi^-$

$K^0_S \to \pi^+\, \pi^-$

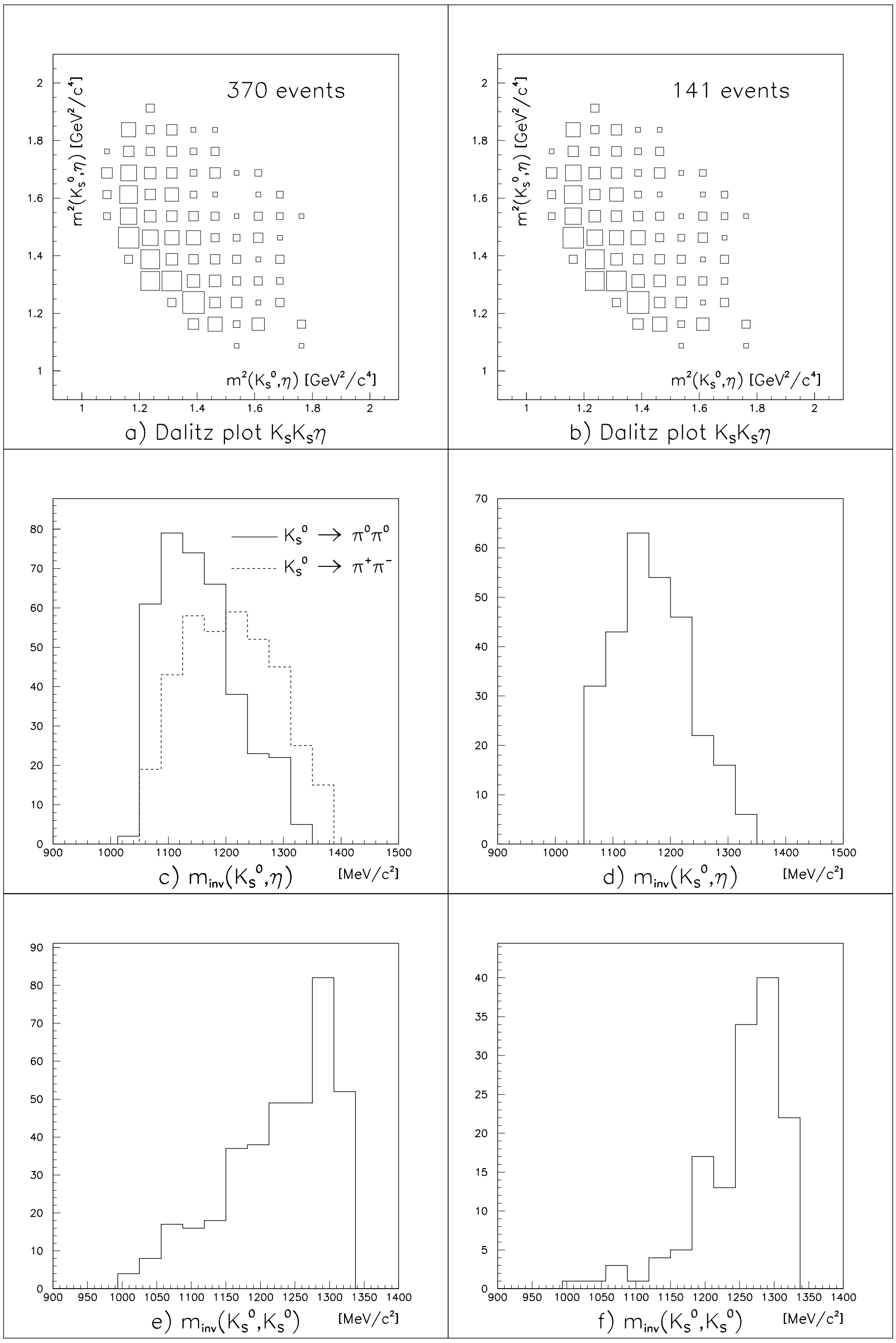

Figure 1.17: *The Dalitz plots of the final state $K^0_S K^0_S \eta$ for the data subsets with one (left column) and two (right column) charged K^0_S-decays and their projections.*

Acceptance correction

An acceptance correction with the use of Monte Carlo data has been done bin by bin requiring a minimum number (at least non zero) of entries per bin. The number of entries in each bin of the experimental Dalitz plot has been divided by the number of entries in the corresponding bin of the Monte Carlo Dalitz plot and the resulting Dalitz plot is normalized so that the total number of events in the acceptance corrected Dalitz plot is equal to the number of experimental data. The error in each bin then consists of the errors in the bins of the experimental and of the Monte Carlo Dalitz plot, the contribution of these two errors to the normalization factor is negligible. All bins with more than 2/3 of their total area outside the phase space limit are excluded of the acceptance correction.

The acceptance corrected Dalitz plots of fig. 1.18a and c are generated only for events with one charged K_S^0-decay. At least 2 entries in case of the Monte Carlo data and 1 entry for the experimental data have been required for these plots.

The acceptance corrected Dalitz plot for the final state $K_S^0 K_S^0 \pi^0$ (fig. 1.18a) looks fairly symmetric apart from the uncertainties in the right corner due to empty bins. The two projections on the $m^2(K\pi)$-axis (fig. 1.18b) are almost identical now within the error bars (compare with fig. 1.16 c).

As to the final state $K_S^0 K_S^0 \eta$ the Dalitz plot contains only 370 events in case of one charged K_S^0-decay leading to a large error of the acceptance correction. Within these large error bars the $K_S^0 K_S^0 \eta$-Dalitz plot is rather symmetric after the acceptance correction (fig. 1.18c and d).

A χ^2-test can be done to check the symmetry quantitatively and the result shows that the acceptance is well understood for both final states.

$$\chi^2_{symmetry} = \sum_{i,j\ ;\ i>j} \frac{(entries\ in\ bin(i,j) - entries\ in\ bin(j,i))^2}{(error\ in\ bin\ (i,j))^2 + (error\ in\ bin\ (j,i))^2} \tag{1.3}$$

$$\chi^2_{symmetry}\ (K_S^0 K_S^0 \pi^0) = 1.22 \quad (bin\ size\ :\ 0.05\ GeV^2/c^4) \tag{1.4}$$

$$\chi^2_{symmetry}\ (K_S^0 K_S^0 \eta) = 1.32 \quad (bin\ size\ :\ 0.10\ GeV^2/c^4) \tag{1.5}$$

$$p\bar{p} \longrightarrow K^0_S K^0_S \pi^0$$

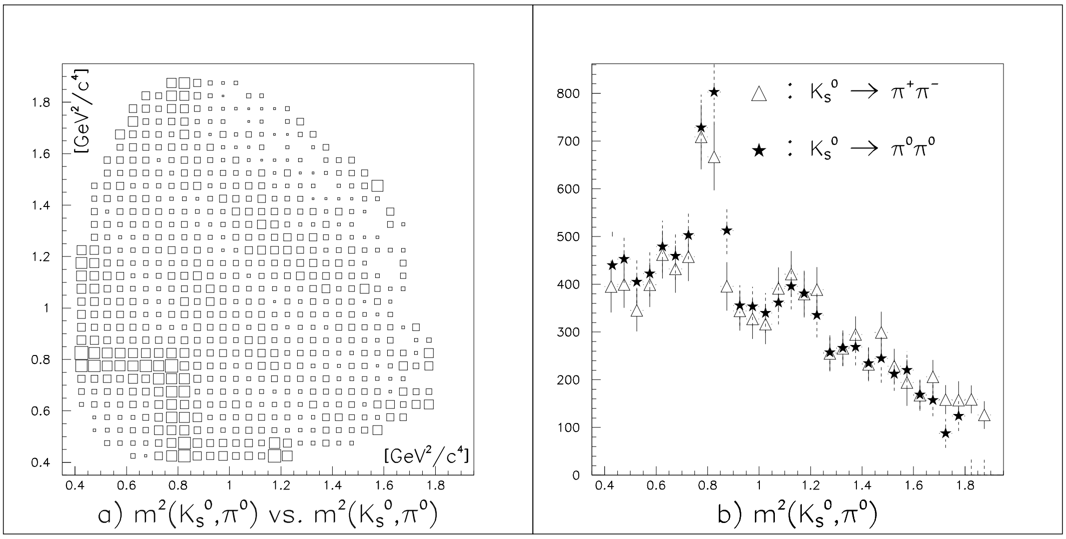

$$p\bar{p} \longrightarrow K^0_S K^0_S \eta$$

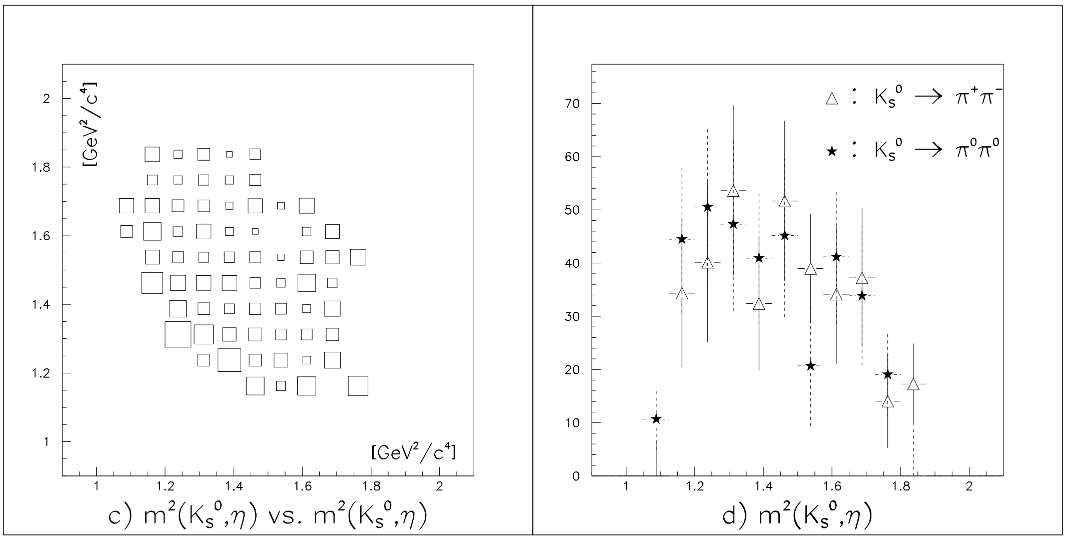

Figure 1.18: **a** *is the acceptance corrected Dalitz plot for the channel* $K^0_S K^0_S \pi^0$ *obtained from events with one charged* K^0_S*-decay and* **b** *are the two projections on* $m^2_{inv}(K^0_S \pi^0\ )$ *which agree very well.* **c** *and* **d** *is the equivalent for the channel* $K^0_S K^0_S \eta$.

Acceptance correction for the final state $K_S^0 K_S^0 \pi^0$ after symmetrization (one charged K_S^0-decay only)

In order to get a maximum of information with a minimal error per bin a symmetric Dalitz plot was produced by simply filling in each event twice (fig. 1.19a). The acceptance correction of this Dalitz plot leads to fig. 1.19b and its projections fig. 1.19c and d. This has been done only for final state $K_S^0 K_S^0 \pi^0$, because the statistics for the final state $K_S^0 K_S^0 \eta$ is too low to do an partial wave analysis using the χ^2-method for a binned data set.

For a Dalitz plot χ^2-fit it is proposed to use the data of fig. 1.19b.

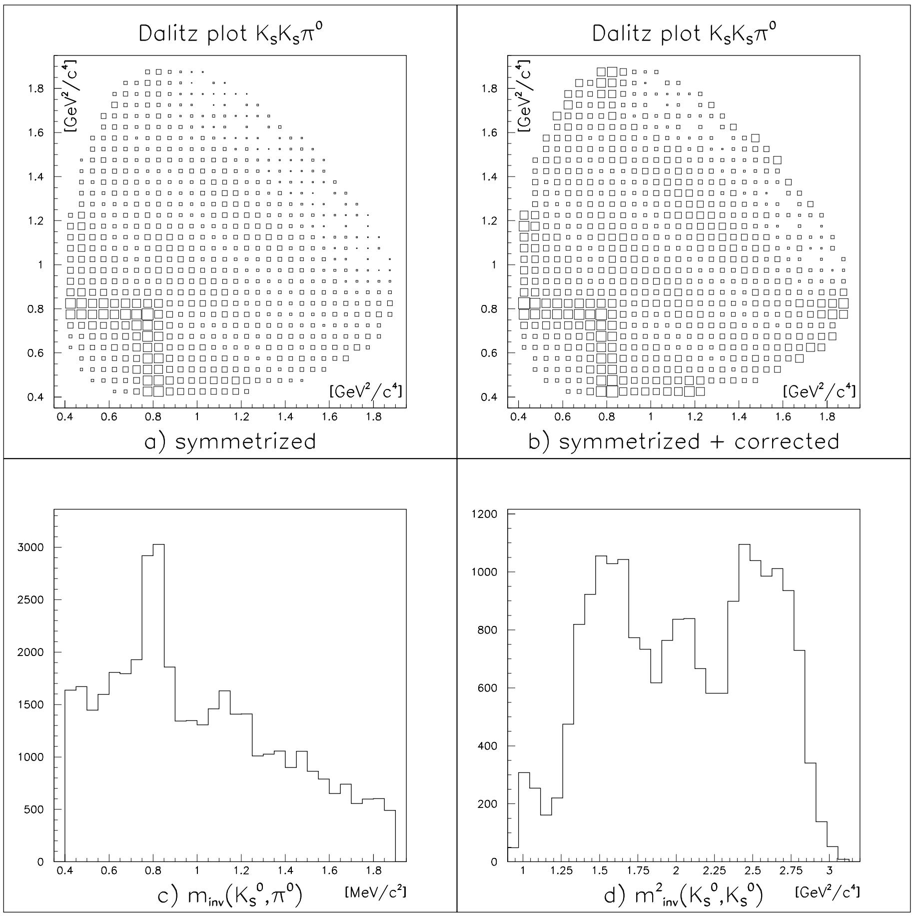

Figure 1.19: **a** *is the Dalitz plot before the correction with two entries per event ('symmetrized') and* **b** *is the same Dalitz plot after the acceptance correction,* **c** *and* **d** *are the projections of* **b**. *Only events with one charged* K_S^0*-decay have been used here.*

2-prong versus 4-prong data

After acceptance correction the two Dalitz plots for the $K_S^0 K_S^0 \pi^0$-data subsets of events with one respectively two charged K_S^0-decays should be in principle identical. However, the compatibility of the two data sets is limited by the low statistics in some areas of the phase space leading to empty bins which cannot be corrected.

Since it makes obviously no sense to do an acceptance correction for empty bins and the correction of very low populated bins suffers from low statistics, the two data sets are only compared for bins which have at least three entries in either of the two Dalitz plots. For a bin size of 0.064 GeV^2 the bins shown in fig. 1.20a have therefore been excluded from the comparison.

A χ^2/bin can be defined to give a quantitative result for the compatibility of the two Dalitz plots DP_1 and DP_2 :

$$\chi^2/bin \;=\; \sum_{i,j} \frac{(entries\ in\ bin\ (i,j)\ of DP_1 - entries\ in\ bin\ (i,j)\ of DP_2)^2}{(error\ in\ bin\ (i,j)\ of DP_1)^2 + (error\ in\ bin\ (i,j)\ of DP_2)^2} \;=\; 1.45 \tag{1.6}$$

This χ^2/bin is fairly satisfactory, but the distribution of bins with $\chi^2 > 3$ (fig. 1.20b) shows still deviations for small $K\overline{K}$-masses, where the acceptance decreases in particular for events with two charged K_S^0-decays, and in some edge bins.

Hence, the conformity of the two $(K\pi)$-projections (fig. 1.20c) is rather good (see the projections in fig. 1.20 c and d) but it seems to be dangerous to mix the two data sets for the partial wave analysis.

The comparison of the two $K\overline{K}$-projections (fig. 1.20d) is a bit misleading since both data sets are normalized so that the total number of entries in both Dalitz plots are equal. The conformity is very well in one part and less good in another part, but the normalization compensate these facts leading to deviations over the whole mass range.

An increased statistics using the 1996-data taken with the SVX-detector as K_S^0-trigger will probably reduce these systematic uncertainties and will make it possible to add the two data sets for the partial wave analysis.

$\boldsymbol{K^0_S K^0_S \pi^0}$ after acceptance correction

$K^0_S K^0_S \longrightarrow \pi^0\ \pi^0\ \pi^+\ \pi^-$ **versus** $K^0_S K^0_S \longrightarrow \pi^+\ \pi^-\ \pi^+\ \pi^-$

(comparison for bins with $\geq$ 3 entries only)

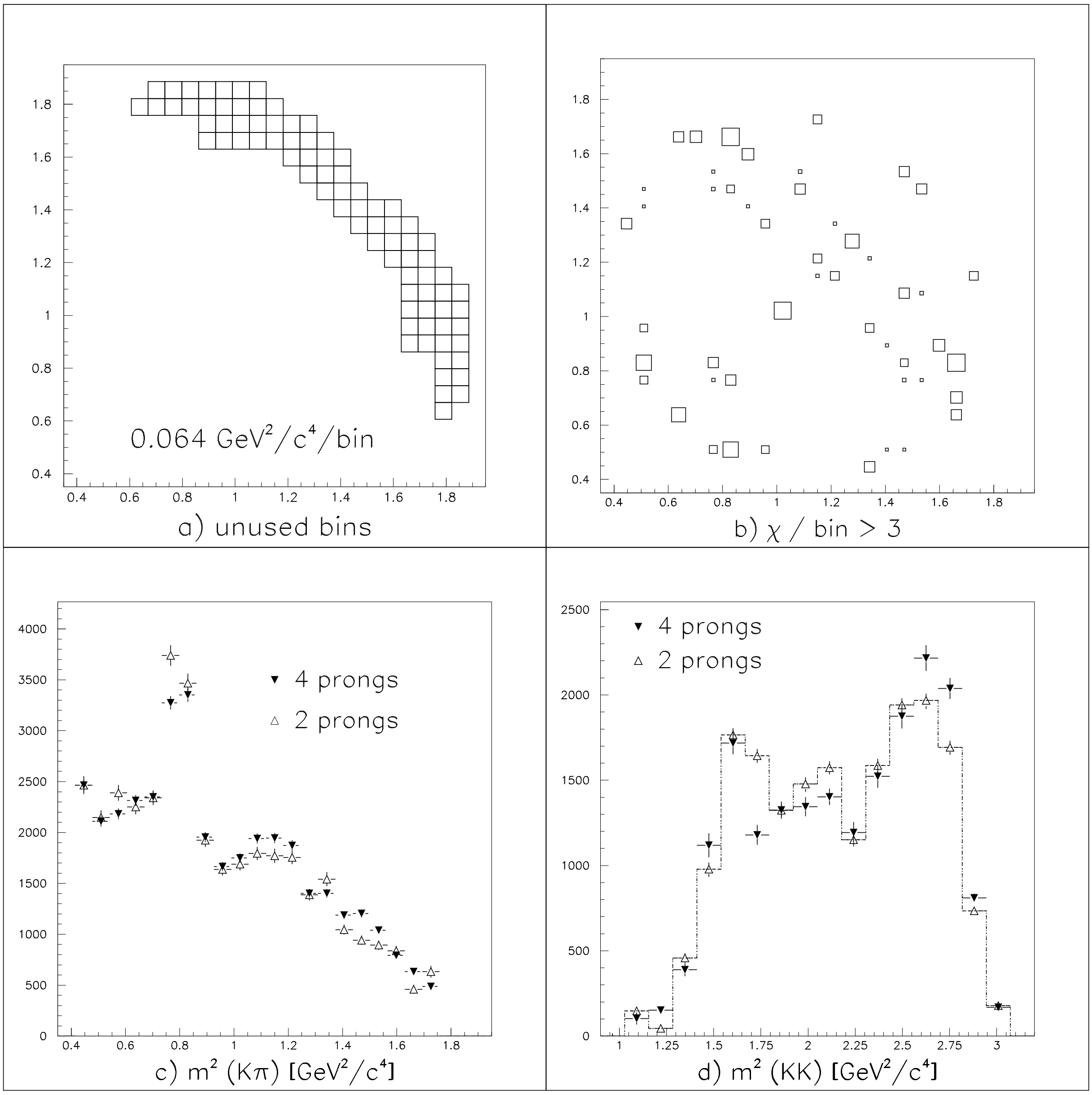

Figure 1.20: *Comparison of the two data subsets* $K^0_S(\pi^0\ \pi^0\ )K^0_S(\pi^+\ \pi^-\ )\pi^0$ *and* $K^0_S(\pi^+\ \pi^-\ )K^0_S(\pi^+\ \pi^-\ )\pi^0$ *. Only bins are compared which have at least one three entries. The* $K\pi$*-projections agree rather good, but there are some discrepancies in the* KK*-projection.*

Chapter 2

The Partial Wave Analysis (PWA)

2.1 The isobar model

The data are analyzed in terms of the isobar model. The initial state is assumed to be pure S-wave and must then be $p\overline{p}$ ($^1S_0$) because $C = +1$ for the $K^0_SK^0_S\pi^0$ final state, hence $J^{PC}(p\overline{p}\ ) = 0^{-+}$.

If X stands for the intermediate state and M_1, M_2 and M_3 for the three mesons of the final state then the isobar model can be sketched as follows :

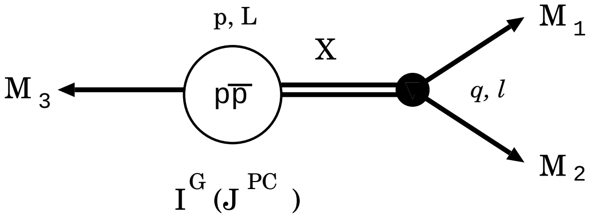

Figure 2.1: *Sketch of the isobar model*

where p denotes the break-up momentum in the $p\overline{p}$ -rest frame with the relative angular momentum L between X and M_3 and q and l the equivalent in the rest frame of the resonance which decays into M_1 and M_2.

The isospin I of the initial state is either 0 or 1 and it is assumed that the amplitudes related to different isospins of the $p\overline{p}$ -system can be added coherently.

Basically there are two possible decay chains :

1. $p\overline{p} \longrightarrow XK^0_S$, $X \longrightarrow K^0_S\pi^0$
2. $p\overline{p} \longrightarrow X\pi^0$, $X \longrightarrow K^0_SK^0_S$

and from that the quantum numbers of all allowed resonances can be deduced (tab. 2.1).

$X \longrightarrow$	l	L	$I(J^{P(C)})(X)$	possible resonances
$K_S^0\pi^0$	0	0	1/2 (0^+)	$(K\pi)_S - wave$
	1	1	1/2 (0^-)	$K^*(892)$
$K_S^0K_S^0$	0	0	0 (0^{++})	$f_0(975),\ f_0(1370),\ f_0(1500)$
	0	0	1 (0^{++})	$a_0(980),\ a_0(1450)$
	2	2	0 (2^{++})	$f_2(1270),\ f_2'(1525)$
	2	2	1 (2^{++})	$a_2(1320)$

Table 2.1: *Possible intermediate states in the reaction* $p\bar{p} \rightarrow K_S^0K_S^0\pi^0$. *Some more resonances are possible according to [1] but less likely.*

The total transition amplitude A_{tot} can be written as the coherent sum over all M partial amplitudes A_k describing the possible intermediate states, therefore the probability density function at the point (s_1, s_2) in the Dalitz plot is

$$W(s_1, s_2, \Lambda_1 ... \Lambda_M) \ = \ |\sum_{k=1}^{M} \Lambda_k A_k(s_1, s_2)|^2 \ \cdot \ \rho_{LIPS} \tag{2.1}$$

where $s_1 = m_{inv}^2(K_S^{0,(1)}, \pi^0\ )$ and $s_2 = m_{inv}^2(K_S^{0,(2)}, \pi^0\ )$ are the Dalitz plot variables and $\Lambda_1 ... \Lambda_M$ complex coefficients which can be written as $\Lambda_k = \alpha_k \cdot e^{i\delta_k}$ and have to be determined by a fit.

ρ_{LIPS} describes the phase space density at the point (s_1, s_2) which is, in particular in the case of a triggered data sample, not constant over the phase space. ρ_{LIPS} can be determined by the use of Monte Carlo data (fig. 2.2).

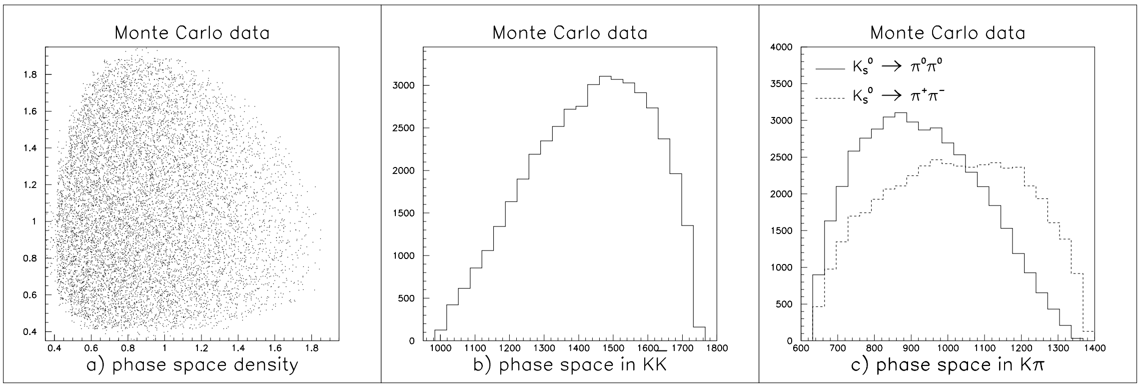

Figure 2.2: *Dalitz plot and projections of the phase space simulation using the Monte Carlo data. This distribution corresponds to* ρ_{LIPS} *in the fit.*

2.2 The maximum likelihood method

From eq. 2.1 a total density function $\mathcal{L}$ can be defined as the product of $W(s_1, s_2, \Lambda_1 ... \Lambda_M)$ over all N_{data} data points normalized to the phase space integral. With $\vec{\Lambda} = (\Lambda_1 ... \Lambda_M)$ this function can be written as :

$$\mathcal{L}(\vec{\Lambda}) = \frac{\prod_{j=1}^{N_{data}} W(s_1^j, s_2^j, \vec{\Lambda})}{\int_{LIPS} W(s_1, s_2, \vec{\Lambda}) ds_1 ds_2} \tag{2.2}$$

The phase space integral $\int_{LIPS}$ can be approximated by the sum over all N_{MC} Monte Carlo data and for simplification $\mathcal{L}$ is replaced by $ln(\mathcal{L})$, so eq. 2.2 can be transformed to

$$ln(\mathcal{L}) = \sum_{j=1}^{N_{data}} ln(W(s_1^j, s_2^j, \vec{\Lambda})) - \sum_{l=1}^{N_{MC}} ln(W(s_1^l, s_2^l, \vec{\Lambda})) \tag{2.3}$$

The parameter set $\vec{\Lambda}$ is now determined by maximizing $ln(\mathcal{L})$:

$$\frac{\partial ln(\mathcal{L})}{\partial \Lambda_k} = 0 \quad ; \quad k = 1...M \tag{2.4}$$

2.3 The helicity formalism

The partial waves A_k are defined in terms of the helicity formalism ([24] and [25]).

With (J, M) being the total spin and its z-component of the initial (and final) state and S_X the spin of the isobar each partial wave amplitude A_k can be written in case of a $p\overline{p}$ -decay into three pseudoscalars as

$$A_k(JM\lambda_1\lambda_2\lambda_3) = (J+1)^{1/2}(S_X+1)^{1/2} \sum_{\lambda_X} D^{J\ *}_{M\lambda_X}(\Phi, \Theta, 0) D^{S_X\ *}_{\lambda_X 0}(\phi, \theta, 0) \cdot f^{J,k}_{\lambda_X} \tag{2.5}$$

In the helicity formalism the momentum vector of a particle produced in a decay is chosen to be the quantization axis, so the helicity is identical to the z-coordinate of its spin in this frame and the transformation is done using the well known rotation D-matrices and the angulars in eq. 2.5 are defined as follows :

- Φ, Θ : azimuthal and polar angle of the isobar momentum vector in the rest frame of the $p\overline{p}$ -annihilation
- ϕ, θ : azimuthal and polar angle of the momentum vector of one of the decay products of the isobar in the rest frame of the isobar with respect to the momentum vector of the isobar in the lab frame.

$f^{J,k}_{\lambda_X}$ is the dynamical part of the k-th partial wave where the helicity of the isobar is connected to its spin S and the angular momentum L of the $p\overline{p}$ -annihilation by Clebsch-Gordan coefficients :

$$f_{\lambda_X}^{J,k} = \sum_{LS} \left(\frac{2L+1}{2J+1}\right)^{1/2} (L0S\lambda_X|J\lambda_X)\ f_{LS}^{J,k} \tag{2.6}$$

The $f_{LS}^{J,k}$ finally are factorized into Blatt-Weisskopf centrifugal-barrier factors as given by Hippel and Quigg [26] and a residual function $\hat{F}(s)$ which depends only on the isobar mass s.

$$f_{LS}^{J,k} = F_L(p)F_J(q)\hat{F}(s) \tag{2.7}$$

using the formulas

$$F_0(p) = 1 \tag{2.8}$$

$$F_1(p) = \left(\frac{2(p/p_R)}{(p/p_R)+1}\right)^{1/2} \tag{2.9}$$

$$F_2(p) = \left(\frac{13(p/p_R)^2}{((p/p_R)-3)^2+9(p/p_R)}\right)^{1/2} \tag{2.10}$$

$p_R \approx\ 0.2GeV/c$ corresponds to an annihilation radius of 1 fermi and the $F_L(p)$ are normalized so that $F_L(p) = 1$ for $p/p_R = 1$.

2.4 The dynamical function

In all the following formulas a dimensionless two-body phase space factor ρ will be used which is connected to the break-up momentum q of the two outgoing particles (masses m_1 and m_2) in the rest frame of the decaying particle (mass m) via the relation

$$\rho(m) = 2q/m = 2/m \cdot \sqrt{(m^2-(m_1+m_2)^2)\,(m^2-(m_1-m_2)^2)}/m \tag{2.11}$$

and

The Breit-Wigner function

For each of the resonances in tab. 2.1 one has to parametrize the dynamical part of eq.2.7. The standard relativistic Breit-Wigner form

$$\hat{F}(s) = \frac{m_0\Gamma_0}{m_0^2 - m^2 - im_0\Gamma(m)} \tag{2.12}$$

with m_0 and Γ_0 being mass and width of the isobar and

$$\Gamma(m) = \Gamma_0 \frac{m_0}{m}\frac{q(m)}{q(m_0)}\frac{F_L^2(q(m))}{F_L^2(q(m_0))} \tag{2.13}$$

can be used for any resonance which has no significant overlap with another resonance which is identical in all quantum numbers (I, G, J, P, C) and if the amplitude is negligible at threshold. In this analysis a Breit-Wigner function was used for the particles in tab. 2.2 whose masses and widths are taken from [1] (except the values for the $a_0(1450)$ which are from [27].

Resonance	$K^*(892)$	$a_0(1450)$	$f_2(1270)$	f_2'(1525)	$a_2(1320)$
Mass $[MeV/c^2]$	896.1	1470	1275	1525	1318
Width $[MeV/c^2]$	50.5	265	185	76	110

Table 2.2: *Resonances described by a Breit-Wigner amplitude. Masses and widths are taken from [1] (except for the* $a_0(1450) \rightarrow$ *[27]*

Fig. 2.3 **d-l** show a phase space simulation of all the Breit-Wigner resonances of tab. 2.2 and the relevant projections where they can preferably be seen in the experimental data (fig. 2.3**a-c**) if they contribute to the total transition amplitude. Since the simulations are done using the Monte Carlo data of fig. 2.2 the effect of the trigger becomes visible in the asymmetries.

Fig. 2.3 **d** and **e** show that the K*K-amplitude is not only responsible for the peaks in the $(K\pi)$-projections (**b**), but also for the strong peak at around 1600 MeV/c^2 in the $(K\overline{K})$-projection and for a part of the peak at around 1200 MeV/c^2 (**c**).

The strong band at the left boundary of the experimental Dalitz plot can be identified with the $f_2'(1525)$ (**f, g**). The effect that this band looks much stronger than the corresponding band at the lower side of the Dalitz plot is due to the accumulation of events with very fast charged decaying K_S^0 by the trigger. Therefore the $f_2'(1525)$ can be seen very clearly in only one $(K\pi)$-projection, whereas it is not showing up in the other one (**b**).

The $a_0(1450)$ (**h, i**) is a very broad object and - if it is coupling to $K\overline{K}$ - it may help to explain the peak in the middle of fig. 2.3 **c**.

The two tensor resonances $f_2(1270)$ and the $a_2(1320)$ are close together and have a similar pattern in the Dalitz plot. In fig. 2.3 **j-l** there are two examples of a phase space simulation using the same ratio of intensities $(I(f_2)/I(a_2) \approx 1/3)$ in both cases, but a relative phase of 0^0 in **j** and of 180^0 in **k**. The two tensors will contribute to the description of the peak at around 1200 MeV/c in the experimental data, the $(K\overline{K})$-projection of the two amplitudes will be smaller if the relative phase is at around 180^0.

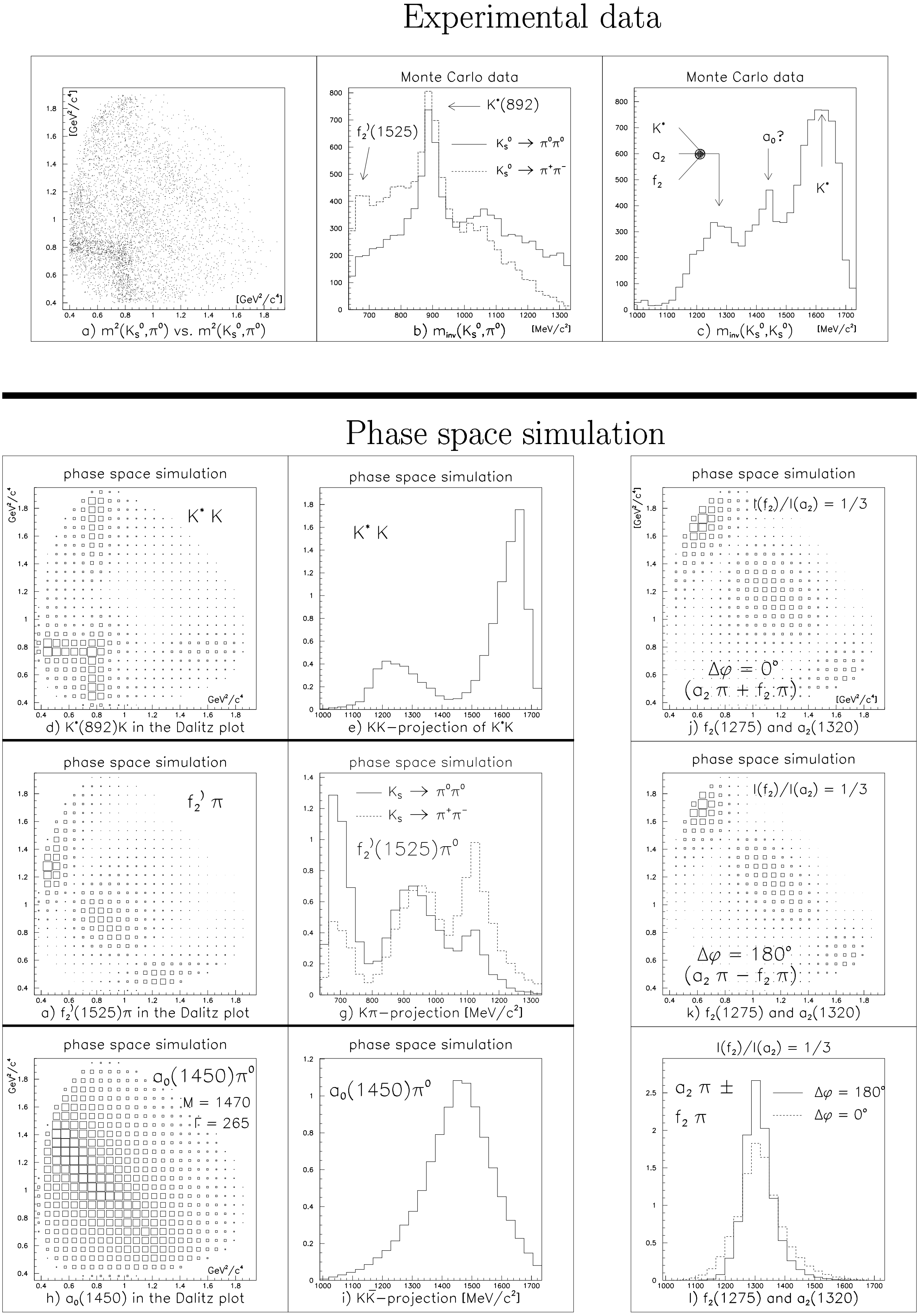

Figure 2.3: *A phase space simulation of the Breit-Wigner resonances of tab. 2.2 helps to associate them with the peaks in the experimental data. The presence of the* $a_0(1450)$ *is not confirmed a priori, the corresponding peak in the* $(K\overline{K})$*-projection could also be explained by the* $(K\overline{K})_S$*-wave with* $I = 0$*, as it will be shown later.*

The Flatté formula ($f_0(975)$ and $a_0(980)$)

For any resonance nearby threshold the standard Breit-Wigner formula is not suitable to describe it correctly. The common formula for the $\mathrm{a}_0(980)$ has been evaluated by S. M. Flatté in a coupled-channel analysis of the decays $\mathrm{a}_0(980) \rightarrow K\overline{K}$ and $\mathrm{a}_0(980) \rightarrow \eta\pi$ [28]. The denominator of eq. 2.12 is changing to

$$m_0^2 - m^2 - im_0 g_{\eta\pi}(q_{\eta\pi} + r \cdot q_{K\overline{K}}) \quad ; \quad r \;=\; \frac{g_{K\overline{K}}}{g_{\eta\pi}} \tag{2.14}$$

$$\Gamma_{tot} \;=\; \Gamma_{K\overline{K}} \;+\; \Gamma_{\eta\pi} \;=\; g_{\eta\pi}q_{\eta\pi} \;+\; g_{K\overline{K}}q_{K\overline{K}} \tag{2.15}$$

Since the parameters $g_{\eta\pi}$ and r turned out to be strongly correlated in the analysis of [28], their values could not be determined accurately. Therefore the values of [29] have been taken for this analysis, where the Crystal Barrel data of $p\overline{p} \rightarrow \omega\eta\pi^0$ at rest [31] have been used as additional information :

$$m_0 \;=\; 999\; MeV/c^2 \quad ; \quad g_{\eta\pi} \;=\; 221\; MeV/c^2 \quad ; \quad r \;=\; 1.16 \tag{2.16}$$

The same type of formula has been used for the $f_0(975)$, but $g_{\eta\pi}$ and $q_{\eta\pi}$ become now $g_{\pi\pi}$ and $q_{\pi\pi}$. The parameters are taken from [30] :

$$m_0 \;=\; 990\; MeV/c^2 \quad ; \quad g_{\pi\pi} \;=\; 270\; MeV/c^2 \quad ; \quad g_{K\overline{K}} \;=\; 116.1\; MeV/c^2 \tag{2.17}$$

Fig. 2.4a shows that it will be difficult to disentangle the two scalars at the $(K\overline{K})$-threshold. If the relative phase between the two amplitudes is 180^0, the resulting amplitude becomes much smaller in the $(K\overline{K})$-projection than the single contributions and the total amplitude goes down to zero very rapidly. Therefore the high mass tail will hardly help to disentangle the two amplitudes by interference effects with amplitudes of higher mass, but on the other hand it will probably not have a dramatic falsifying effect on other amplitudes if one assumes only one scalar at threshold as a first approximation.

Fig. 2.4b is a simple phase space simulation of the $a_0(980)$ with the parameters of 2.16 which is chosen for the fits. It becomes clear that for fitting a binned data set a careful inclusion of the edge bins is very crucial.

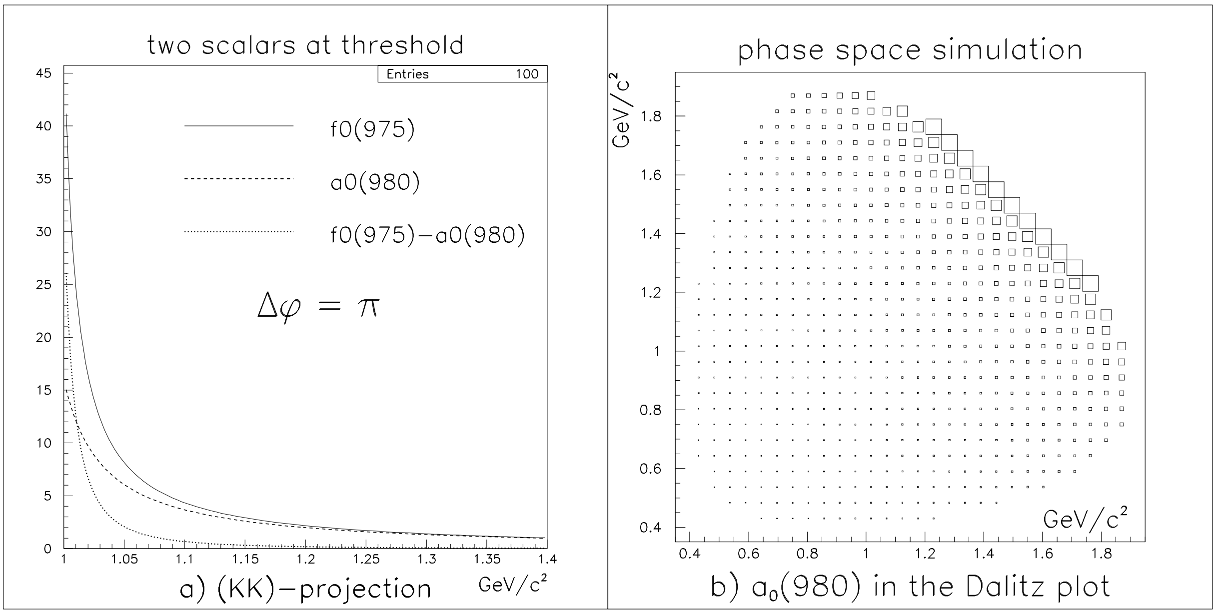

Figure 2.4: *The phase space simulation shows that both* $f_0(975)$ *and* $a_0(980)$ *have a long tail to higher masses, but the two tails can cancel out each other completely if the relative phase is around* 180^0. *The resulting signal is then similar to a single Flatté-resonance but much more narrow (***a***). The example in* **b** *shows that most of the* a_0*-signal is found in the edge bins of the Dalitz plot. If one likes to bin the data for a fit one has to be aware of this fact.*

The $(K\pi)_S$-wave

From the LASS experiment the scattering amplitude $\mid T \mid$ and the phase shift δ for $(K\pi)_S$-scattering is known [32]. The $(K\pi)_S$-wave can be parametrized as the sum of a resonance pole and a background term in terms of an effective range approximation.

$$\hat{K} = \frac{m_0\Gamma_0/\rho(m_0)}{m_0^2 - m^2} + \frac{am}{2 + abq^2} \tag{2.18}$$

where $m_0/\Gamma_0 = 1.332/0.401\ GeV/c^2$ are the mass and the width of the resonance, $a = 1.79(GeV/c)^{-1}$ the scattering length and $b = 3.46(GeV/c)^{-1}$ the effective range. The values are obtained by a fit from K. Braune [33]. They differ slightly from the values given in [35].

The $(K\overline{K}_S)$-wave with $I = 0$ (P-vector approach)

From [34] we know that - apart from the $f_0(975)$ - there are two isoscalar resonances with $J^{PC} = 0^{++}$ within the phase space of the $K_S^0 K_S^0 \pi^0$-channel and since they overlap

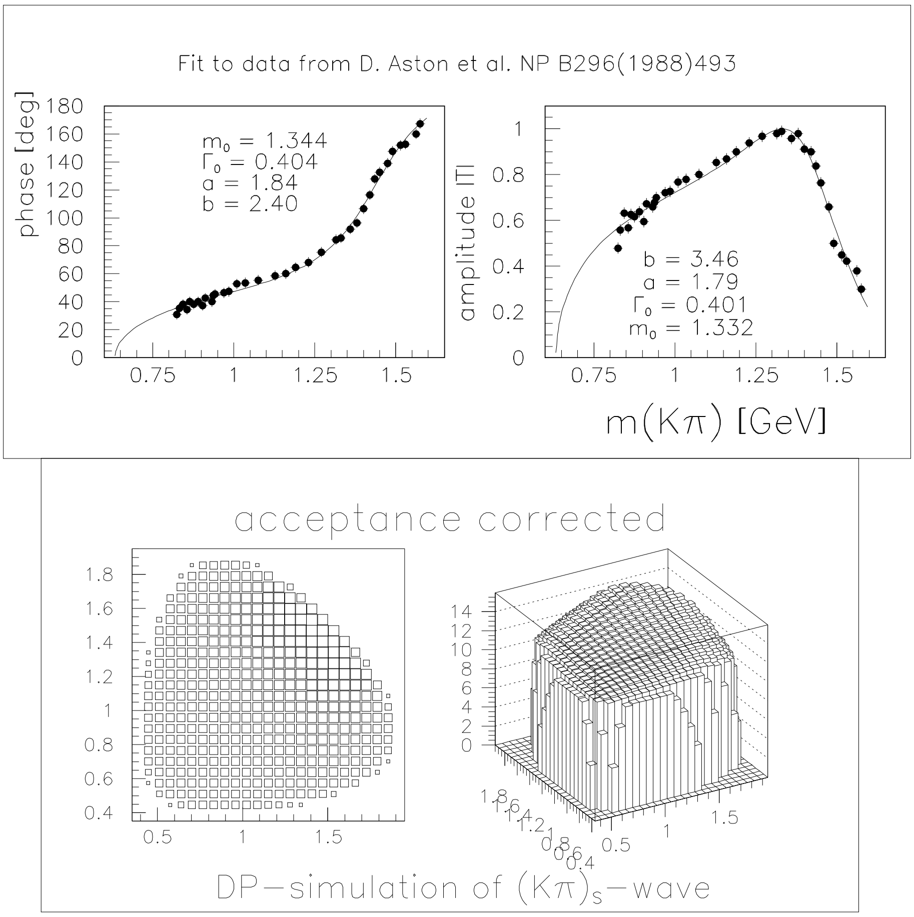

Figure 2.5: *The data for the $(K\pi)_S$-wave from the LASS experiment [32] and the parameters of eq. 2.18 from a fit by K. Braune [33]. In this analysis the parameters from the fit of the amplitude are used.*
The simulation of the $(K\pi)_S$-wave distribution in the Dalitz plot is acceptance corrected for better visualization.

significantly one has to describe these two poles in terms of the K-matrix formalism which guarantees unitarity in the two-particle scattering amplitude.

In this analysis only one decay channel $(K\overline{K})$ is allowed for the resonances, therefore the K-matrix becomes a simple scalar function :

$$\hat{K} = \frac{m_1\Gamma_1/\rho_1(m_1)}{m_1^2 - m^2} + \frac{m_2\Gamma_2/\rho_2(m_2)}{m_2^2 - m^2} \tag{2.19}$$

m_1 and m_2 are the masses of the resonances and Γ_1 and Γ_2 their widths. The helicity amplitudes and the damping factors are equal to 1 in this case. The masses and widths in eq. 2.19 are those of the K-matrix poles and they are related to the resonance parameters of the T-matrix via

$$\hat{T} = (I - i\rho\hat{K})^{-1}\hat{K} \tag{2.20}$$

The values for the T-Matrix poles can be obtained by a scan of $\hat{T}$ in the complex energy plane [36].

The production of the isobars in the $p\bar{p}$ -annihilation can be described by the introduction of a $\hat{P}$-vector [37] which has to have the same poles as the K-matrix. The coupling parameters β_1 and β_2 to the $p\bar{p}$ -vertex are assumed to be constant, i.e. independent of the energy.

$$\hat{P} = \beta_1 \cdot \frac{m_1\Gamma_1/\rho_1(m_1)}{m_1^2 - m^2} + \beta_2 \cdot \frac{m_2\Gamma_2/\rho_2(m_2)}{m_2^2 - m^2} \tag{2.21}$$

The dynamical function $\hat{\mathrm{F}}$ can now be written as

$$\begin{aligned} \hat{F} = \ (I - i\rho\hat{K})^{-1}\hat{P} \ = \ & \beta_1 \cdot \frac{m_1\Gamma_1/\rho_1(m_1)}{m_1^2 - m^2 - i\rho_1(m_1\Gamma_1/\rho_1(m_1) + \Delta_{12})} + \\ & \beta_2 \cdot \frac{m_2\Gamma_2/\rho_2(m_2)}{m_2^2 - m^2 - i\rho_2(m_2\Gamma_2/\rho_2(m_2) + \Delta_{21})} \end{aligned} \tag{2.22}$$

which differs from the sum of two Breit-Wigner functions by the additional overlap terms

$$\begin{aligned} \Delta_{12} &= \frac{m_1^2 - m^2}{m_2^2 - m^2} \cdot \frac{m_2\Gamma_2}{\rho_2(m_2)} \\ \Delta_{21} &= \frac{m_2^2 - m^2}{m_1^2 - m^2} \cdot \frac{m_1\Gamma_1}{\rho_1(m_1)} \end{aligned} \tag{2.23}$$

2.5 Fit program for the PWA

The coefficients of the total transition amplitude are fitted using the program MAXTOOL [39] which includes a slightly modified version of SPIN [40]. Using the unbinned experimental and Monte Carlo data sets a loglikelihood is defined as in eq. 2.3 and its maximum is obtained using the CERN package MINUIT [41].

Intensities

The phase space integral of the total transition amplitude is normalized to 1. The intensity of a single resonance is calculated by setting all complex coefficients to zero except for this amplitude where the coefficient is taken from the fit. The integral of this amplitude over the phase space is replaced by the sum over all Monte Carlo data (chap. 2.2). Due to interference effects the sum of the individual intensities is not equal to the intensity of the sum of all amplitudes.

The intensity of the $(K\overline{K})_S^{I=0}$-wave is the integral of the right side of eq. 2.22 with β_1, β_2 from the fit, but also the individual production strength of each of the two poles can be defined as the integral of the respective part of this amplitude.

Errors

All errors of intensities and phases in the next chapter correspond to the MINOS error analysis of MINUIT [41] whereas the errors of the K-matrix pole parameters are mainly obtained by scanning the loglikelihood versus one of the four pole parameters while setting the other three to different fixed values. The absolute loglikelihood for the best fits was always around $ln = 1755$ and it turned out that already a decrease of 10 (absolute value) causes the fit to be obviously worse.

Generally the $(K\overline{K})$-projection will be used to compare the fit with the data. This turned out to be more suitable to see where the fit goes wrong compared to a posteriori generated χ^2-Dalitz plots, since the latter ones are strongly affected by the trigger effects (low acceptance in parts of the phase space leads to a low number of entries and fake a good χ^2 in these bins).

2.6 Fit results

2.6.1 The $K\overline{K}_S$-wave with $I = 0$

As starting values the K-Matrix poles of [42] have been used :

- Pole 1 : $M_1 = 1361\ MeV/c^2$; $\Gamma_1 = 264\ MeV/c^2$
- Pole 2 : $M_2 = 1571\ MeV/c^2$; $\Gamma_2 = 162\ MeV/c^2$

For the first ('basic') fit the $a_0(1450)$ was excluded and only one amplitude in terms of a Flatté parametrization (the parameters of $a_0(980)$ as given in chap. 2.4) was used for a $K\overline{K}$-resonance at threshold. $K^*(892)$, $f_2(1270)$, $a_2(1320)$ and $f_2'(1525)$ are included in terms of Breit-Wigner functions and the $(K\pi)_S$-wave as described in chap. 2.4.

The dominant contribution in this fit comes from the two poles of the $(K\overline{K})_S^{I=0}$-wave and from K$^*K$, the intensities of all the other amplitudes are not strong but significant (tab. 2.3). The description of the data is already quite good, but in particular the $(K\overline{K})$-projection shows that improvements are necessary (fig. 2.6).

'basic' fit : $ln(\mathcal{L}) = 1740$					
K-matrix	M $[MeV/c^2]$	Γ $[MeV/c^2]$	T-matrix	M $[MeV/c^2]$	Γ $[MeV/c^2]$
Pole 1	1361	264	Pole 1	1402	346
Pole 2	1571	162	Pole 2	1516	98

Intermediate state	I [%]	ϕ $[deg]$	Intermediate state	I [%]	ϕ $[deg]$
$(K\overline{K})_S^{I=0}\pi^0$ Pole 1	43.1 ± 5.4	118.0 ± 2.3	$a_0(980)\pi^0$	2.7 ± 0.6	159.7 ± 4.2
$(K\overline{K})_S^{I=0}\pi^0$ Pole 2	23.4 ± 3.6	153.6 ± 3.5	$f_2(1270)\pi^0$	4.4 ± 0.6	329.7 ± 4.6
K$^*(892)K$	15.7 ± 1.4	0.0_{fixed}	$a_2(1320)\pi^0$	5.5 ± 0.5	103.5 ± 2.9
$(K\pi)_S K$	3.2 ± 1.1	230.0 ± 6.3	$f_2'(1525)\pi^0$	2.9 ± 0.4	111.5 ± 3.9

Table 2.3: *Result of the 'basic' fit. The intensities are calculated using the definition given in chap. 2.5, the phase of* K$^*K$ *is fixed at* 0^0. *The T-matrix poles are obtained by a scan of* T *(calculated via eq. 2.20) in the complex energy plane.*

Starting from this result the pole parameters of the $(K\overline{K})_S^{I=0}$-wave have been varied and the effect on the fit has been investigated. It turned out that the parameters of the higher mass pole are very stable when varying the parameters of the other pole. As an example the loglikelihood is plotted versus the mass M_2 (fig. 2.7a) and the width Γ_2 (fig. 2.7b) for different values of Γ_1 and a fixed pole mass $M_1 = 1364\ MeV/c^2$.

A variety of such scans has been done and - defining an error by the change of the loglikelihood of approximately $ln(\mathcal{L})_{max} \pm 5$ - the parameters of the higher mass pole are determined to

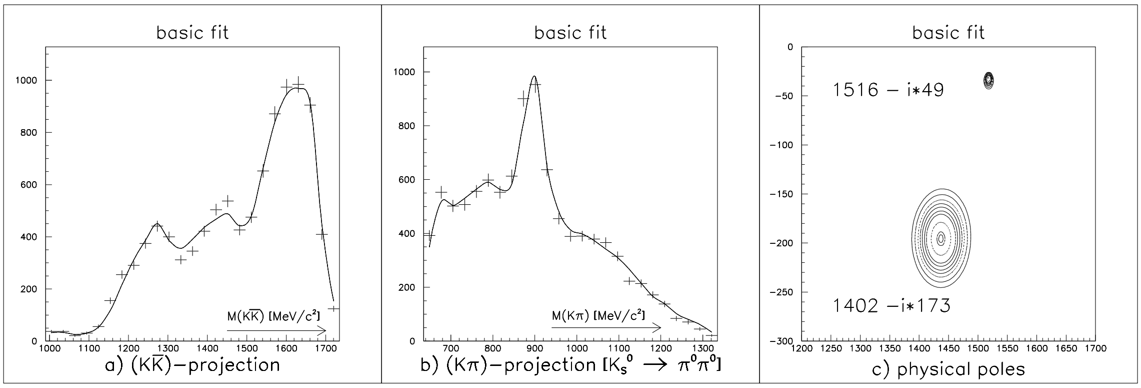

Figure 2.6: *The 'basic' fit using the same pole parameters and the same resonances as in [42] leads to a result which is not far from the best solution, but there are still some problems in the ($K\overline{K}$)-projection around the $f_0(1370)$ (error bars for the experimental data, solid line for the fitted amplitude).*

- $M_2 \;=\; 1576^{+16}_{-7}\; MeV/c^2 \quad ; \quad \Gamma_2 \;=\; 175 \pm 15\; MeV/c^2$

As to the lower mass pole it is expected to peak around $1380 MeV/c^2$ in the T-matrix. The peak in the middle of the $K\overline{K}$-projection (fig. 2.6a), however, is at a higher mass, at around $1440 MeV/c^2$.

Leaving the pole parameters free in the fit leads to the K-matrix pole $1389 - i255 MeV/c^2$ which is slightly higher in mass than before. The increase in $ln(\mathcal{L})$ from 1740 to 1755 and the $(K\overline{K})$-projection show that the data are now much better described by the fit.

A more systematic investigation of the errors leads to an optimum for the K-matrix pole of

- $M_2 \;=\; 1389^{+8}_{-13}\; MeV/c^2 \quad ; \quad \Gamma_2 \;=\; 255 \pm 23\; MeV/c^2$

The T-matrix poles are obtained from the K-matrix poles by a scan of eq. 2.20 over the complex energy plane. The errors of the T-matrix pole are derived from different scans with variation of the K-matrix poles within their errors.

Using the pole parameters and the coefficients for the $(K\overline{K})^{I=0}_{S}$-wave from the fit a Dalitz plot can be simulated only for the 2-pole 1x1 K-matrix. A projection of this Dalitz plot is shown in fig. 2.9 for the T-vector (eq. 2.20) and for the F-vector (eq. 2.22). In both cases the shape of the $(K\overline{K})^{I=0}_{S}$-wave can be explained by a broad component with a peak at around 1440 MeV/c^2 and a small component leading to the dip at 1510 MeV/c^2 and shifting the lower peak to a lower mass (about 1370 MeV/c^2).

Any attempt to fit the data with a T-matrix mass of the broad object below 1400 MeV/c^2 failed.

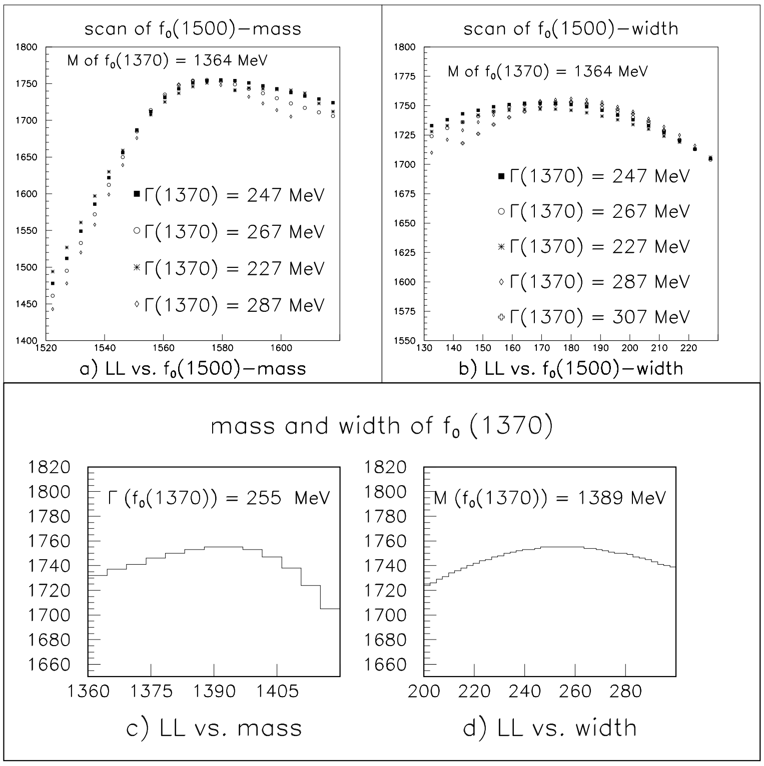

Figure 2.7: *The loglikelihood of the fit for different fixed values of the* $(K\overline{K})_S^{I=0}$*-pole parameters. For the higher mass pole the maxima are rather independent of variations of the parameters of the lower mass pole (a and b).*

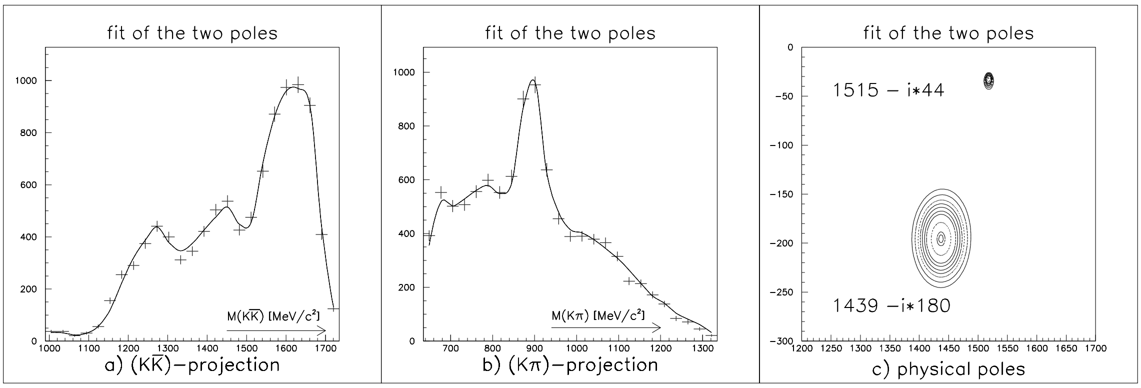

Figure 2.8: *Projections of the experimental data (error bars) and of the fit result (solid line) after fitting the K-matrix poles of the* $(K\overline{K})_S^{I=0}$*-wave. The description of the data is now much better in the* $(K\overline{K})$*-projection (***a***) than for the basic fit (fig. 2.6a). The* $(K\pi)$*-projection is shown for the neutral decaying* K_S^0*, where the signal of the* $f_2'(1525)$ *can be seen (***b***). The T-matrix pole of the* $f_0(1370)$ *is now at a significantly higher mass than before.*

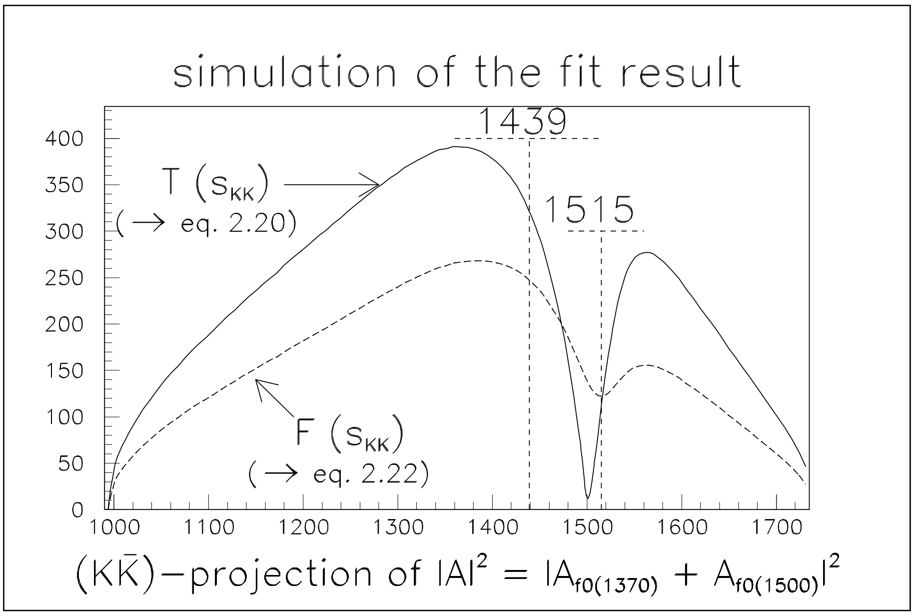

Figure 2.9: *Simulation of the $(K\overline{K})$-projection of the $(K\overline{K})_S$-wave with the pole parameters obtained by the fit. The broad pole peaks at* 1439 MeV/c^2 *but the overlapping small resonance which causes the dip at* 1515 MeV/c^2 *makes the peak appear at a lower mass in the $(K\overline{K})$-projection.*

Fit of the poles : $ln(\mathcal{L}) = 1755$					
K-matrix	M $[MeV/c^2]$	Γ $[MeV/c^2]$	T-matrix	M $[MeV/c^2]$	Γ $[MeV/c^2]$
Pole 1	1389^{+8}_{-13}	255 ± 23	Pole 1	1439^{+10}_{-20}	360 ± 50
Pole 2	1576^{+16}_{-7}	175 ± 15	Pole 2	1515 ± 5	88^{+15}_{-5}

Intermediate state	I [%]	ϕ $[deg]$	Intermediate state	I [%]	ϕ $[deg]$
$(K\overline{K})_S^{I=0}\pi^0$ Pole 1	48.5 ± 6.1	131.4 ± 2.3	$a_0(980)\pi^0$	3.5 ± 0.8	179.1 ± 8.4
$(K\overline{K})_S^{I=0}\pi^0$ Pole 2	31.8 ± 4.0	162.3 ± 1.9	$f_2(1270)\pi^0$	4.4 ± 0.6	340.4 ± 7.0
$\mathrm{K}^*(892)K$	16.9 ± 1.6	0.0_{fixed}	$a_2(1320)\pi^0$	4.5 ± 0.8	118.0 ± 5.4
$(K\pi)_S K$	2.3 ± 1.8	204.3 ± 8.2	$f_2'(1525)\pi^0$	3.3 ± 0.3	117.3 ± 3.4

Table 2.4: *The fit of the K-matrix poles leaves the upper mass pole rather stable, but the lower mass pole moves up slightly in mass. This results in a T-matrix pole with a significantly larger mass for the lower mass pole than used in the basic fit (tab. 2.3).*

The $(K\overline{K})_S$-wave in terms of two Breit-Wigner functions

So far the $(K\overline{K})_S$-wave has been fitted in terms of a 1x1 K-matrix because it was assumed that the two scalars have equal isospin ($I = 0$). The fit, however, is not sensitive on the isospin of a particle, therefore it is not excluded that the two scalars have different isospin.

Assuming different isospin the two scalars have to be fitted in terms of two Breit-Wigner functions and it turned out that the data can be described in an equally good way. Also the masses and the widths of the two poles are almost identical with those obtained by the 1x1 K-matrix fit. The production rates, however, differ strongly in both cases.

The upper mass pole can naturally be assigned to the $f_0(1500)$, and the only reasonable explanation would then be to assign the other pole to the $a_0(1450)$. However, it turned out that using fixed values of mass and width of the $a_0(1450)$ (1470/265 MeV/c^2 [27]) makes the fit worse. The change in $ln(\mathcal{L})$ is not big but the result indicates that the lower mass pole is not compatible with the $a_0(1450)$ observed in $\eta\pi^0\pi^0$.

Moreover the intensity of the $a_0(1450)$ in $K^0_S K^0_S \pi^0$can be predicted from the results of the $\eta\pi^0\pi^0$-channel to $(7.7 \pm 2.1)\%$ [35] and this is far away from the results of tab. 2.5.

Therefore it is the best explanation to assume two scalars with the same isospin and to fit the data in terms of a 1x1 K-matrix. If they are assumed to have zero isospin they can be naturally identified as the well known $f_0(1370)$ and $f_0(1500)$.

Fit with two Breit-Wigner poles					
	$M[MeV/c^2]$	$\Gamma[MeV/c^2]$	I [%]	$\phi[deg]$	$ln(\mathcal{L})$
Pole 1 fitted	1431 ± 4.7	332 ± 16.3	64.7 ± 9.3	131.6 ± 2.0	1754
Pole 2 fitted	1520 ± 2.3	98 ± 7.4	12.2 ± 3.0	41.6 ± 6.6	
$a_0(1450)$ (pole fixed)	1470	265	97.5 ± 21.4	161.2 ± 1.5	1747
$f_0(1500)$ (pole fixed)	1520	98	22.6 ± 4.9	29.0 ± 1.4	

Table 2.5: *Result of a fit with two Breit-Wigner amplitudes instead of the 1x1 K-matrix. In the lower case where the values of [27] for the* $a_0(1450)$ *have been fixed for the lower mass pole the broad object dominates the fit but the description of the data gets slightly worse.*

2.6.2 The $(K\overline{K})_S$-wave with $I = 1$

The mass and width of the $a_0(1450)$ have been taken from [27] :

- $M \; = 1470 \; MeV/c^2 \quad ; \quad \Gamma \; = \; 265 \; MeV/c^2$ **fixed !**

Using the pole position for the $f_0(1500)$ as obtained in chap. 2.6.1 the pole parameters for the $f_0(1370)$ have been fitted with different fixed intensities for the $a_0(1450)$.

It turns out that with any intensity between 0 % and 25 % the data can be described in an equally good way, i.e. the loglikelihood for the best fit does not change (fig. 2.10a). The pole parameters of the $f_0(1500)$ are stable, the mass of the $f_0(1370)$ is slightly decreasing with increasing $a_0(1450)$-contribution and its width is increasing significantly (fig. 2.10a and b).

Fig. 2.10c shows that the total intensity of the $(K\overline{K})_S^{I=0}$-wave integrated over the whole phase space is decreasing strongly with an increasing intensity of the $a_0(1450)$ and so do the two components of the $(K\overline{K})_S^{I=0}$-wave individually (for the last two values the two components of eq. 2.22 have been separated and integrated individually over the phase space). The intensity of the total $(K\overline{K})_S$-wave, including the $a_0(1450)$, is approximately constant for any intensity of the $a_0(1450)$.

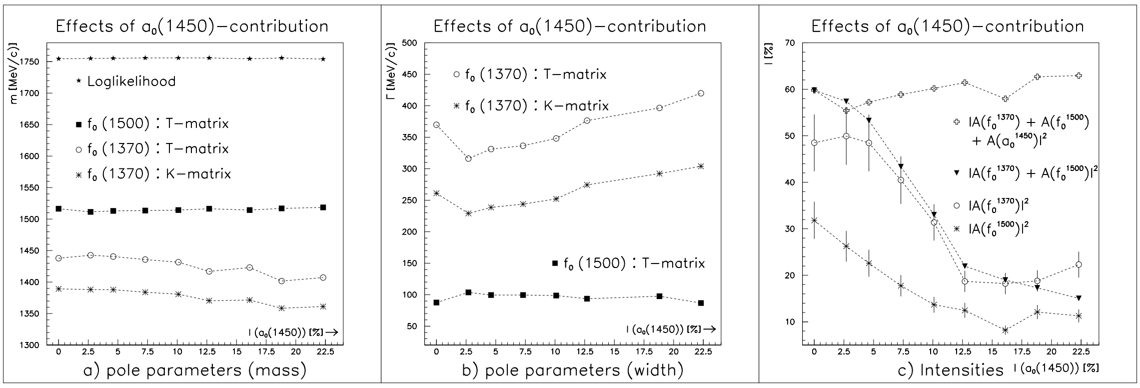

Figure 2.10: *A variation of the $a_0(1450)$ between 0% and 25% does not change the loglikelihood of the best fit (***a***). The mass of the $f_0(1370)$ is decreasing slightly and its width increasing significantly whereas the pole of the $f_0(1500)$ remains stable (***a*** and ***b***).*
*The intensity for the total $(K\overline{K})_S$-wave is approximately constant for any $a_0(1450)$-contribution between 0 and 25 % (***c***). The total intensity for the component with $I = 0$ is decreasing as well as for the two intensities of the two single parts of the $(K\overline{K})_S^{I=0}$-wave.*

The branching ratio $BR(p\overline{p} \rightarrow f_0\pi^0 \rightarrow K\overline{K}\pi^0)$ can now be derived for each of the two poles of the $(K\overline{K})_S^{I=0}$-wave. Taking into account a factor 4 for the isospin and using the total branching ratio of $p\overline{p} \longrightarrow K_S^0 K_S^0 \pi^0$ of [43] it can be calculated via

$$BR \; (p\overline{p} \rightarrow f_0\pi^0 \rightarrow K\overline{K}\pi^0 \;) \; = \; 4 \cdot \; (7.5 \pm 0.3) \; \cdot 10^{-4} \; \cdot \; I(f_0\pi^0 \; in \; K_S^0 K_S^0 \pi^0) \qquad (2.24)$$

The results are shown in fig. 2.11 and tab. 2.6. In particular the values for the $f_0(1500)$ agree very well with those of [35] and [42], for the $f_0(1370)$ not all are within 1σ, but the differences are not dramatic. Taking into account the fact that the results are obtained from two data sets with completely different signatures in the experiment, hence two completely different reconstruction techniques, and that two different fit methods have been used fort the two partial wave analyses, the compatibility of the results are extremely satisfactory.

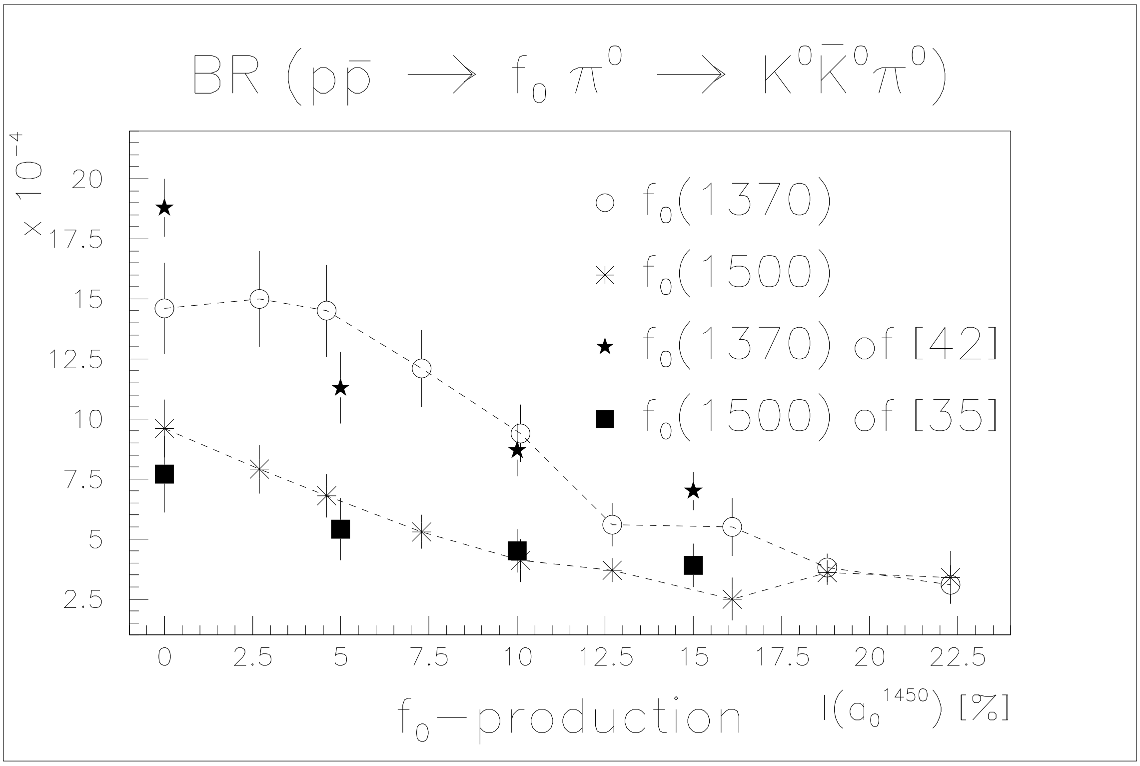

Figure 2.11: *The product branching ratios $BR(p\overline{p} \to f_0(1370)\pi^0 \to K\overline{K}\pi^0)$ and $BR(p\overline{p} \to f_0(1500)\pi^0 \to K\overline{K}\pi^0)$ of the two parts of the 1x1 K-matrix separately are decreasing with increasing contribution of the $a_0(1450)$. The values for the $f_0(1500)$ agree very well with those of [35] and [42], for the $f_0(1370)$ they differ slightly but not dramatically.*

Intensity of $a_0(1450)$ [%]	$BR(p\overline{p} \longrightarrow f_0(1370)\pi^0\ )\times$ $BR(f_0(1370)\rightarrow K\overline{K})[10^{-4}]$	$BR(p\overline{p} \longrightarrow f_0(1500)\pi^0\ )\times$ $BR(f_0(1500)\rightarrow K\overline{K})[10^{-4}]$
0.0	14.6 ± 1.9	9.6 ± 1.2
2.7	15.0 ± 2.0	7.9 ± 1.0
4.6	14.5 ± 1.9	6.8 ± 0.9
7.3	12.1 ± 1.6	5.3 ± 0.7
10.2	9.4 ± 1.6	4.1 ± 0.9
12.7	5.6 ± 0.9	3.7 ± 0.5
16.1	5.5 ± 1.2	2.5 ± 0.9
18.8	3.8 ± 0.6	3.6 ± 0.5
22.3	3.1 ± 0.8	3.4 ± 1.1

Table 2.6: *The product branching ratios $BR(p\overline{p} \rightarrow f_0(1370)\pi^0 \rightarrow K\overline{K}\pi^0)$ and $BR(p\overline{p} \rightarrow f_0(1500)\pi^0 \rightarrow K\overline{K}\pi^0)$ for different $a_0(1450)$-intensities. All values are compatible within 1σ with the results of the channel $K^0_L K^0_L \pi^0$ (table 1 of [35], table 23 and figure 66 of [42]).*

The relative couplings of $f_0(1370)$ and $f_0(1500)$ to $\pi\pi$ and $K\overline{K}$ can now be obtained by the use of eq.(13) of ref. [45] :

$$\frac{BR(p\overline{p} \rightarrow f_0\pi^0 \rightarrow K\overline{K}\pi^0)}{BR(p\overline{p} \rightarrow f_0\pi^0 \rightarrow 3\pi^0)} = \frac{\Gamma_{K\overline{K}}}{\Gamma_{\pi\pi}/3} = \frac{\gamma^2_{K\overline{K}} \cdot |F_{K\overline{K}}(\vec{q})|^2 \cdot S_{K\overline{K}}(\vec{q})}{\gamma^2_{\pi\pi} \cdot |F_{\pi\pi}(\vec{q})|^2 \cdot S_{\pi\pi}(\vec{q})} \cdot 3 \qquad (2.25)$$

Note that the isospin factor 4 for $K\overline{K}$was already introduced in eq. 2.24.
With the definitions of [45]

$$S(\vec{q}) = q \ ; \ |F(\vec{q})|^2 = exp(-q^2/8\beta^2) \ ; \ \beta \simeq 0.5\,GeV/c \qquad (2.26)$$

and q being the break-up momentum of f_0 in $\pi\pi$ respectively $K\overline{K}$, eq. 2.25 turns into

$$\frac{\gamma^2_{K\overline{K}}}{\gamma^2_{\pi\pi}} = \frac{1}{3} \cdot \frac{BR(p\overline{p} \rightarrow f_0\pi^0 \rightarrow K\overline{K}\pi^0) \cdot q_{\pi\pi} \cdot |F_{\pi\pi}(\vec{q})|^2}{BR(p\overline{p} \rightarrow f_0\pi^0 \rightarrow 3\pi^0) \cdot q_{K\overline{K}} \cdot |F_{K\overline{K}}(\vec{q})|^2} \qquad (2.27)$$

With the masses of $f_0(1370)$ and $f_0(1500)$ of tab. 2.4 and the known branching ratios $BR(p\overline{p} \rightarrow f_0\pi^0 \rightarrow 3\pi^0)$ the relative couplings can now be calculated. For the product branching ratio of $f_0(1370)$ and $f_0(1500)$ in $3\pi^0$ the values of [44] are taken in order to compare the results with those from the channel $K^0_L K^0_L \pi^0$, but it has to be pointed out that the values for $f_0(1370)$ are an upper limit only and both values are larger in [27]. Moreover, the product branching ratio for the $f_0(1370)$ in the $3\pi^0$-final state is a factor of four smaller in [46].

The dotted line in fig. 2.12 and fig. 2.13 refer to the predictions $\gamma^2_{K\overline{K}}/\gamma^2_{\pi\pi} = 1/3$ for a pure $u\overline{u} + d\overline{d}$-state from [45] and $I(a_0(1450)) = (7.7 \pm 2.1)\%$ [35].

Intensity of $a_0(1450)$ [%]	$f_0(1370)$ $\gamma^2_{K\overline{K}}/\gamma^2_{\pi\pi}$	$f_0(1500)$ $\gamma^2_{K\overline{K}}/\gamma^2_{\pi\pi}$
0.0	$> 0.226 \pm 0.045$	0.458 ± 0.081
2.7	$> 0.233 \pm 0.047$	0.377 ± 0.072
4.6	$> 0.226 \pm 0.045$	0.325 ± 0.054
7.3	$> 0.189 \pm 0.038$	0.255 ± 0.043
10.2	$> 0.146 \pm 0.034$	0.296 ± 0.046
12.7	$> 0.087 \pm 0.019$	0.179 ± 0.040
16.1	$> 0.085 \pm 0.023$	0.112 ± 0.030
18.8	$> 0.059 \pm 0.014$	0.174 ± 0.039
22.3	$> 0.048 \pm 0.014$	0.162 ± 0.047

Table 2.7: *The relative couplings* $\gamma^2_{K\overline{K}}/\gamma^2_{\pi\pi}$ *for the* $f_0(1370)$ *and* $f_0(1500)$ *for different* a_0*-intensities. For each case an equally good fit could be obtained.*

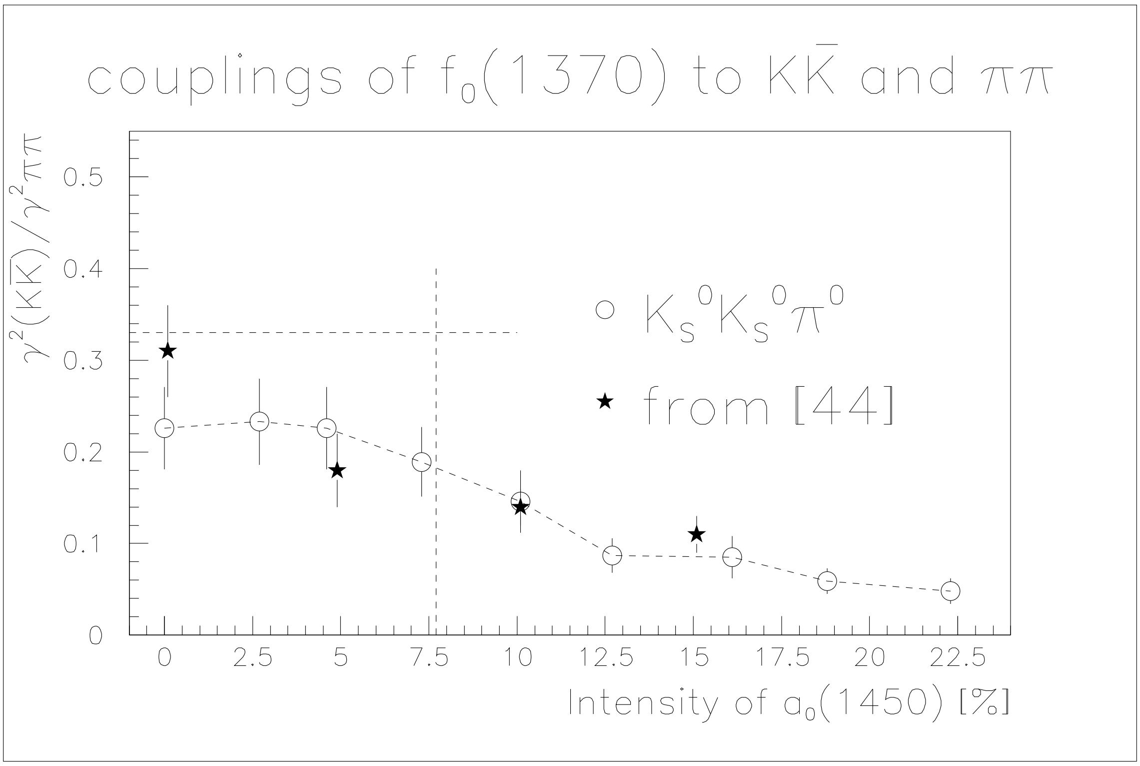

Figure 2.12: *The relative couplings* $\gamma^2_{K\overline{K}}/\gamma^2_{\pi\pi}$ *for the* $f_0(1370)$ *as a function of the* a_0*-contribution (see tab. 2.7 for exact values). The predictions for* $\gamma^2_{K\overline{K}}/\gamma^2_{\pi\pi}$ *from [45] and* $I(a_0(1450)) = 7.7\%$ *[35] are marked by the dotted lines.*

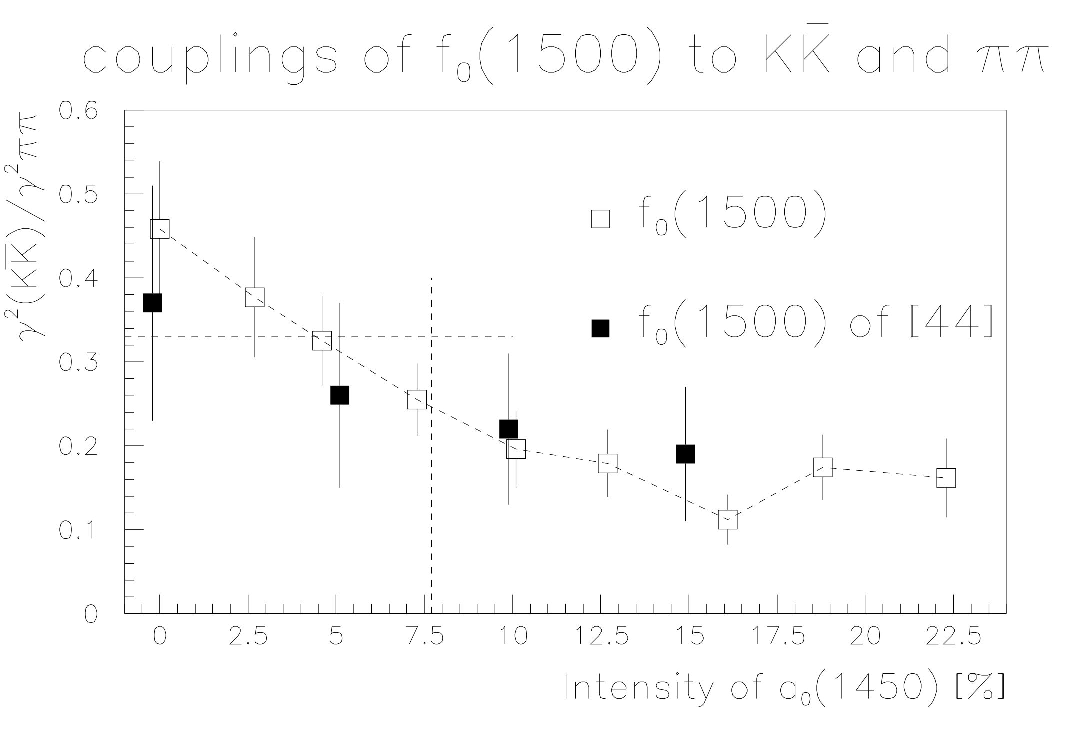

Figure 2.13: *The relative couplings* $\gamma^2_{K\overline{K}}/\gamma^2_{\pi\pi}$ *for the* $f_0(1500)$ *as a function of the* a_0*-contribution (see tab. 2.7 for exact values). The predictions for* $\gamma^2_{K\overline{K}}/\gamma^2_{\pi\pi}$ *from [45] and* $I(a_0(1450)) = 7.7\%$ *[35] are marked by the dotted lines.*

2.6.3 The isoscalar $f_0(975)$ and the isovector $a_0(980)$ at threshold

A weak but clear signal can be seen in the $K\overline{K}$-projection near threshold (fig. 2.3c). In chap. 2.4 it was shown that from the $K^0_S K^0_S \pi^0$-data alone it seems impossible to disentangle the $f_0(975)$ and the $a_0(980)$, therefore an additional information from another channel is necessary.

The best candidate is the channel $K^0_{S/L} K^\pm \pi^\mp$ because here only isovectors are allowed in $K\overline{K}$. From $K^0_S K^\pm \pi^\mp$ [52] an intensity of the $a_0(980)$ of $(2.7 \pm 1.2)\%$ can be predicted for the channel $K^0_S K^0_S \pi^0$which is close to the result in tab. 2.4. Fixing the intensity of the $a_0(980)$ to this number and adding the $f_0(975)$ gives infact a slight increase of the loglikelihood (from 1755 to 1763) with an intensity of $(3.0 \pm 0.4)\%$ for the $f_0(975)$. This indicates a slight significance for two scalars at threshold decaying into $K\overline{K}$.

The pole position of the $f_0(1370)$ was fitted again with $f_0(975)$, once without the $a_0(980)$ and once with the intensity fixed at 2.7 %. In both cases the pole of the $f_0(1370)$ was stable as well as its intensity.

2.6.4 $p\overline{p} \longrightarrow K^*(892)K$

The isospin parts $\Phi^{\epsilon}_{I_{p\overline{p}},i_{K\pi}}$ of the transition amplitude from the $p\overline{p}$ -initial state with $I = 0$ respectively $I = 1$ for $p\overline{p}$ $(^1S_0)$ into the final state $K^0_SK^0_S\pi^0$via $(K\pi)$-coupling can be written as [38]

$$\Phi^{+}_{0,1/2} = -\frac{1}{\sqrt{12}}\Big((K^0\pi^0\ )\overline{K^0}\ + (\overline{K^0}\pi^0\ )K^0\Big) \tag{2.28}$$

$$\Phi^{+}_{1,1/2} = -\frac{1}{2}\Big((K^0\pi^0\ )\overline{K^0}\ + (\overline{K^0}\pi^0\ )K^0\Big) \tag{2.29}$$

The self-interference of the K*-bands is constructive for both the initial states $I = 0$ and $I = 1$. Therefore the transitions from different $p\overline{p}$ -isospin via the K*-resonance cannot be distinguished and hence only one K^*K-amplitude was used in the fit.

In the case of the $p\overline{p}$ -initial state $^1S_0$ the two angular momenta of the subsequent decays are $l = L = 1$ leading to a factor $cos^2\theta$ in the decay amplitude. The influence of this factor on the K*-bands is shown in fig. 2.3d which is a phase space simulation of the decay chain $p\overline{p} \longrightarrow K^*K \longrightarrow K^0_SK^0_S\pi^0$.

The relative phase between the K^*K-amplitude and most of the other amplitudes is roughly $(180 \pm 40)^0$, hence strong destructive interference effects are expected. However, the other amplitudes cross the K^*-band in regions where the K^*K-amplitude itself is around zero, or relatively small. In the region where the K^*K-amplitude is strong - the region where the two K*-bands cross each other - it is hardly affected by other amplitudes. Therefore the pattern of the K^*K in the experimental data is not due to interference effects but due to the $cos^2\theta$-angular distribution.

A fit of the mass and the width of the K^* has been done and the result is compatible with the values of [1] (tab. 2.2)

- $m = 893.6 \pm 1.1\ MeV/c^2$, $\Gamma = 54.0 \pm 2.3\ MeV/c^2$

The contribution of the K^*K-amplitude was extremely stable in all fits :

$$I\ (K^*(892)K\ in\ K^0_SK^0_S\pi^0) = \int_{DP} |A(K^*(892)K) + A(KK^*(892))|^2 = (16.8 \pm 1.6)\ \% \tag{2.30}$$

For the total branching ratio of $p\overline{p}$ $(^1S_0)$ - both isospins $I = 0$ and 1 included, since they cannot be distinguished - into $K^*_0(892)K$ a factor 12 takes all possible decay modes into account and the result is approximately identical to the sum of the branching ratios from $I = 0$ and $I = 1$ separately which was obtained in a coupled channel analysis including $K^0_1K^{\pm}\pi^{\mp}$ [38].

$$\begin{aligned} BR(p\overline{p}\ (^1S_0, I = 0,1) \rightarrow K^*_0(892)K) &= (15.1 \pm 1.6) \cdot 10^{-4} \\ f^{+0}_{K^*K}\ +\ f^{+1}_{K^*K} &= (15.0 \pm 3.0) \cdot 10^{-4} \end{aligned} \tag{2.31}$$

2.6.5 $p\overline{p} \longrightarrow (K\pi)_S K$

The parametrization for the $(K\pi)_S$-wave has originally been derived from the results of the LASS experiment (chap. 2.4). It consists of a high mass pole and an additional background term in an effective range approximation and these two parts are connected by the K-matrix formalism.

The LASS experiment produced the $(K\pi)_S$-wave in K^-p-scattering, the couplings of the two terms to $p\overline{p}$, however, are expected to be different. Moreover it was pointed out that the sensitivity of the LASS experiment below 1 GeV/c^2 is extremely questionable [47] so that there is no reason to adhere to their rigid form. Therefore it is not clear a priori whether the effective range term is infact significant.

For a fit without the $a_0(1450)$ the total contribution of the $(K\pi)_S$-wave is $(2.3\pm1.8)\%$. This value is relatively stable for increasing $a_0(1450)$-contribution. Leaving out the $(K\pi)_S$-wave in the fit without decreases the loglikelihood from 1755 to 1732. The effect of the $(K\pi)_S$-wave can be seen by comparing the $K\overline{K}$-projections of fig. 2.14a with fig. 2.14b where the $(K\pi)_S$-wave was dropped from the fit. This shows that the $(K\pi)_S$-wave is a weak amplitude, but its interference with other amplitudes - in particular with the $(KK)_S^{I=0}$-wave - over the whole phase space makes it an important ingredient for the description of the data.

Now the effective range term was dropped and the $(K\pi)_S$-wave was described by the pole term only. The loglikelihood increased from 1755 to 1766 and the description of the $K\overline{K}$-projection improved slightly in particular in that region where the $f_0(1370)$-amplitude is strong (fig. 2.14c). The intensity of the $(K\pi)_S$-wave increased to $(2.9\pm1.6)\%$. A scan of the loglikelihood versus the scattering length a (fig. 2.14d) shows clearly that the fit improves when a goes to zero leading to a best fit for $a = 0$. The same result was found in the channel $p\overline{p} \rightarrow K_L^0 K^\pm \pi^\mp \pi^0$ [48].

The situation becomes much more complicated if the $(K\pi)_S$-wave is fitted with two different production parameters for the pole and for the effective range term. Both objects are very broad and they cancel out by destructive interference in most part of the phase space. The total $(K\pi)_S$-wave looks now much different than the amplitude of LASS (Dalitz plot simulations fig. 2.15). The fitted $(K\pi)_S$-wave is infact not much different of that from a pole term with large $(K\pi)$-mass. It is a striking feature that the individual contributions of the pole and the effective range term are quite strong (27 % and 12 %) but the intensity of the total $(K\pi)_S$-wave is again rather weak (6 %).

The fit is of course slightly better now since the fit has more parameters ($\Delta(ln\mathcal{L}) = +20$, see the $K\overline{K}$-projection in fig. 2.16), but it turns out that the intensities of all the other amplitudes do not change very much if the $(K\pi)_S$-wave is introduced in that way (tab. 2.8) and also the pole position of the $f_0(1370)$ is not affected.

The $(K\pi)_S$-wave is a very difficult object since the two individual components are very broad and interfere with any other amplitude, but for practical reasons it seems justified to use the pole term only for the fit.

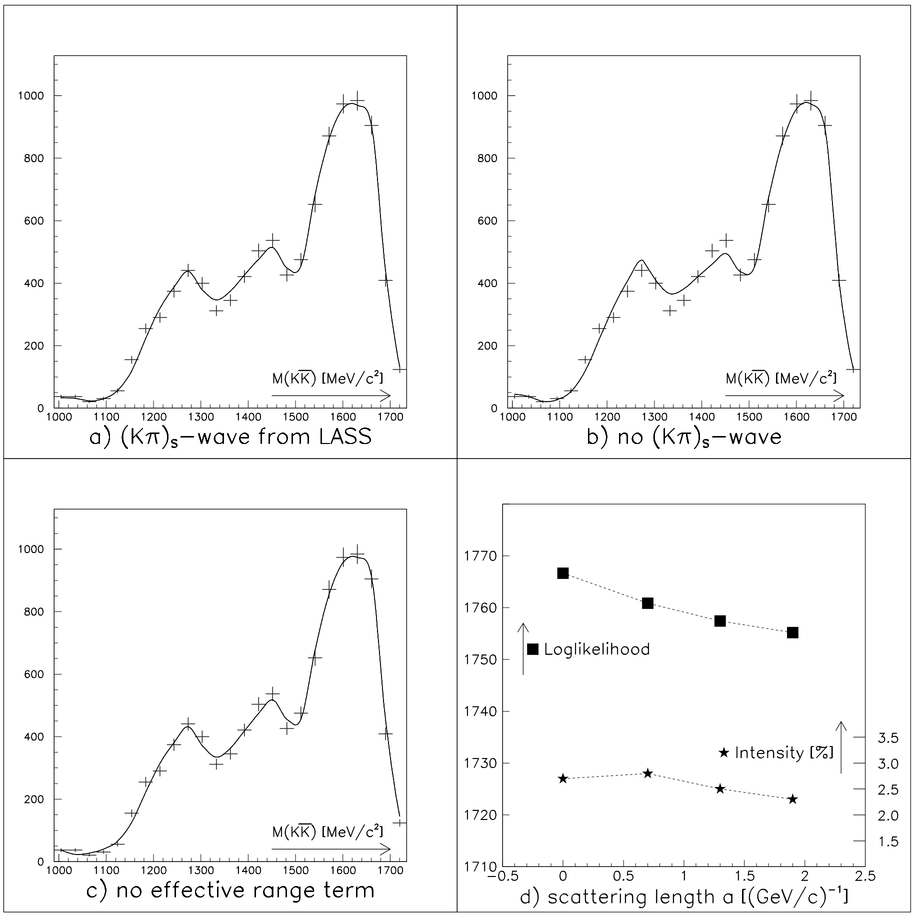

Figure 2.14: *If one leaves out the $(K\pi)_S$-wave from the fit the description of the data gets worse. The fit improves however when the effective range term is dropped.*

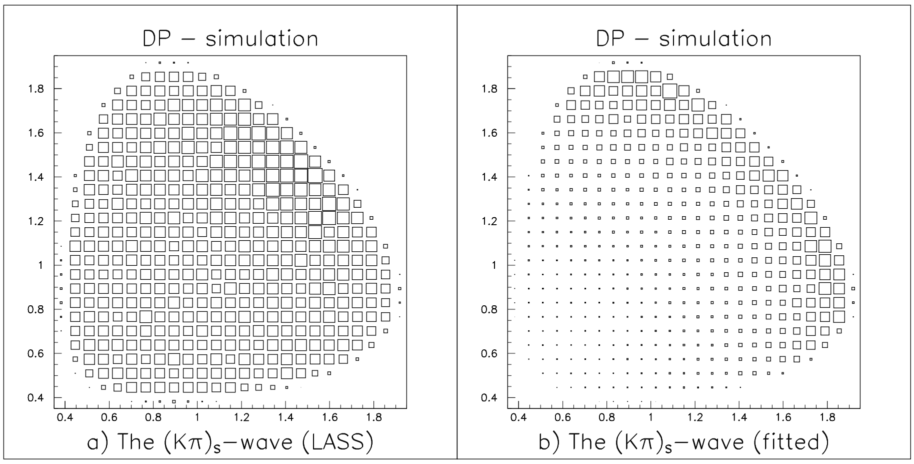

Figure 2.15: *Dalitz plot simulations for the $(K\pi)_S$-wave from LASS and of the fit with two independent production parameters.*

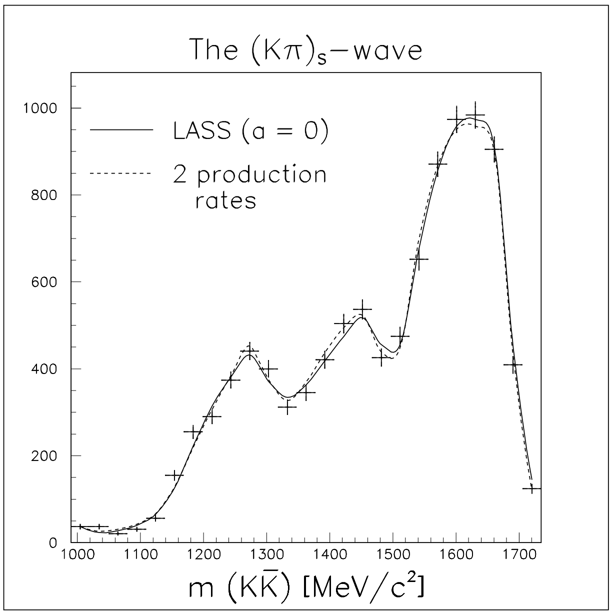

Figure 2.16: *The description of the* $K\overline{K}$*-projection is slightly better with two independent production parameters for the* $(K\pi)_S$*-wave.*

Amplitude	$(K\pi)_S$-wave from LASS	2 production rates
$f_0(1370)\pi^0$	$(48.5 \pm 6.1)\%$	$(49.2 \pm 8.6)\%$
$f_0(1500)\pi^0$	$(31.8 \pm 4.0)\%$	$(34.2 \pm 6.0)\%$
$K^*(892)K$	$(16.9 \pm 1.6)\%$	$(18.0 \pm 4.4)\%$
$(K\pi)_S K$	$(2.3 \pm 1.8)\%$	$(6.0 \pm 1.4)\%$
$a_0(980)\pi^0$	$(3.5 \pm 0.8)\%$	$(1.8 \pm 0.5)\%$
$f_2(1270)\pi^0$	$(4.4 \pm 0.6)\%$	$(2.0 \pm 0.7)\%$
$a_2(1320)\pi^0$	$(4.5 \pm 0.8)\%$	$(9.2 \pm 2.0)\%$
$f_2'(1525)\pi^0$	$(3.3 \pm 0.3)\%$	$(3.5 \pm 1.0)\%$

Table 2.8: *The introduction of two production parameters for the* $(K\pi)_S$*-wave does not affect the other amplitudes very much. Only the* $a_0(980)$ *is now suppressed and the* $a_2(1320)$*-amplitude is about a factor of two larger.*

2.6.6 The tensor mesons $f_2'(1525)$, $f_2(1270)$ and $a_2(1320)$

$f_2'(1525)$

In [35] the first observation of $f_2'(1525)$ in $p\overline{p}$ -annihilation was reported, so it is natural to expect it in the final state $K_S^0K_S^0\pi^0$, too. Infact $ln(\mathcal{L})$ drops from 1755 to 1544 if one leaves out this amplitude in the fit.

It may be surprising that a resonance with not more than 3% contribution to the total amplitude has such a strong effect on the fit quality, but from the phase space simulation of the $f_2'(1525)$-amplitude (fig. 2.17a) one clearly sees that the $f_2'(1525)$ is responsible for the band at the left side of the Dalitz plot (fig 2.3a). The fact that the respective band to be expected on the lower boundary cannot be seen is an effect of the trigger. Thus the $f_2'(1525)$ has a visible effect on the $K\pi$-projection (fig. 2.3b and g), namely an enhancement below the strong K*-peak.

Since the phase space simulation of fig. 2.17a was done with the Monte Carlo data of fig. 2.2a the trigger bias plays an important role in this plot. The trigger accumulates events with a large momentum of the charged decaying K_S^0 and thus intensifies the signal in the corresponding area of the Dalitz plot.

Leaving out the $f_2'(1525)$ makes the fit go wrong in exactly the area where its contribution is expected (fig. 2.17b).

A free fit of mass and width of the $f_2'(1525)$ leads to

- $m \;=\; 1531.9 \pm 2.9\ MeV/c^2 \quad , \quad \Gamma \;=\; 78.3 \pm 13.0\ MeV/c^2$

These values are in good agreement with [1] ($M = (1525 \pm 5) MeV/c^2, \Gamma = (76 \pm 10) MeV/c^2$).

The contribution of the $f_2'(1525)$ is extremely stable for any intensity of the $a_0(1450)$ between 0 and 25 % :

$$I\ (f_2'(1525)\pi^0\ in\ K_S^0K_S^0\pi^0) \;=\; (3.3\ \pm\ 0.4)\% \tag{2.32}$$

From that the branching ratio of $p\overline{p}$ into $f_2'(1525)\pi^0$ can be deduced :

$$\begin{aligned} BR\ (p\overline{p} \longrightarrow f_2'(1525)\pi^0\ ) &= \frac{4 \cdot BR\ (p\overline{p} \rightarrow K_S^0K_S^0\pi^0) \cdot I(f_2'(1525)\pi^0\ in\ K_S^0K_S^0\pi^0)}{BR\ (f_2'(1525) \longrightarrow K\overline{K})} \\ &= \frac{4 \cdot (7.5 \pm 0.3) \cdot 10^{-4} \cdot (0.033 \pm 0.004)}{0.888 \pm 0.031} \\ &= (1.13 \pm 0.13) \cdot 10^{-4} \end{aligned} \tag{2.33}$$

This value is in good agreement with [35] ($(9.38 \pm 1.49) \cdot 10^{-4}$), but the new value for $BR\ (f_2'(1525) \longrightarrow K\overline{K})$ (0.888 instead of the former value 0.712 [1]) was used. The error of the f_2'-intensity is the average of the errors of the fits with different $a_0(1450)$-intensities.

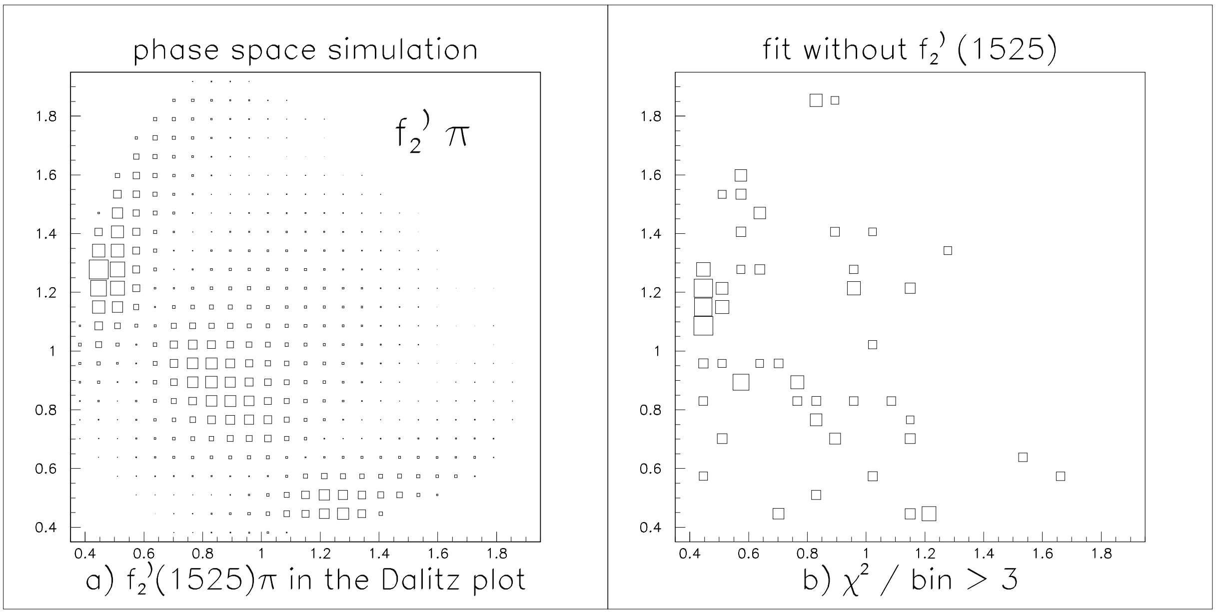

a) $f_2'(1525)\pi$ in the Dalitz plot

b) χ^2 / bin > 3

Figure 2.17: *The* $f_2'(1525)$ *in the Dalitz plot :* **a** *is a pure phase space simulation of its structure in the Dalitz plot and* **b** *the distribution of* χ^2*/bin (if* > 3*) when fitting without the* $f_2'(1525)$*. This clearly proves the importance of a tensor at this mass decaying into* $K\overline{K}$*.*

$a_2(1320)$ and $f_2(1270)$

The contribution of the two tensor mesons $f_2(1270)$ and $a_2(1320)$ in the channel $K^0_S K^0_S \pi^0$can basically be derived from the results of the channels $3\pi^0$ and $\eta\pi^0\pi^0$. The correlations are given by the following equations [49] :

$$BR\ (p\overline{p} \rightarrow f_2\pi^0) = \frac{BR(p\overline{p} \rightarrow 3\pi^0) \cdot I(f_2\pi^0\ in\ 3\pi^0)}{1/3 \cdot BR(f_2 \rightarrow \pi\pi)} \tag{2.34}$$

$$BR\ (p\overline{p} \rightarrow f_2\pi^0) = \frac{BR(p\overline{p} \rightarrow K^0_S K^0_S \pi^0) \cdot I(f_2\pi^0\ in\ K^0_S K^0_S \pi^0)}{1/4 \cdot BR(f_2 \rightarrow K\overline{K})} \tag{2.35}$$

and

$$BR\ (p\overline{p} \rightarrow a_2\pi^0) = \frac{BR(p\overline{p} \rightarrow \eta\pi^0\pi^0) \cdot I(a_2\pi^0\ in\ \eta\pi^0\pi^0)}{1/3 \cdot BR(a_2 \rightarrow \pi\pi)} \tag{2.36}$$

$$BR\ (p\overline{p} \rightarrow a_2\pi^0) = \frac{BR(p\overline{p} \rightarrow K^0_S K^0_S \pi^0) \cdot I(a_2\pi^0\ in\ K^0_S K^0_S \pi^0)}{1/4 \cdot BR(a_2 \rightarrow K\overline{K})} \tag{2.37}$$

Therefore

$$I(f_2\pi^0\ in\ K^0_S K^0_S \pi^0) = \frac{3 \cdot BR(f_2 \rightarrow K\overline{K}) \cdot BR(p\overline{p} \rightarrow 3\pi^0)}{4 \cdot BR(f_2 \rightarrow \pi\pi) \cdot BR(p\overline{p} \rightarrow K^0_S K^0_S \pi^0)} \cdot I(f_2\pi^0\ in\ 3\pi^0) \tag{2.38}$$

$$I(a_2\pi^0 \ in \ K_S^0K_S^0\pi^0) \ = \ \frac{3 \cdot BR(a_2{\rightarrow}K\overline{K}) \cdot BR(p\overline{p} \rightarrow \eta\pi^0\pi^0)}{4 \cdot BR(a_2{\rightarrow}\pi\pi) \cdot BR(p\overline{p} \rightarrow K_S^0K_S^0\pi^0)} \cdot I(a_2\pi^0 \ in \ \eta\pi^0\pi^0) \quad (2.39)$$

This leads - the branching ratios of eqs. 2.38 and 2.39 are taken from [1] and [50] - to the following predictions :

$$I(f_2(1270)\pi^0 \ in \ K_S^0K_S^0\pi^0) \ = \ (4.7 \pm 1.7) \ \% \quad (2.40)$$
$$I(a_2(1320)\pi^0 \ in \ K_S^0K_S^0\pi^0) \ = \ (23.1 \pm 0.6) \ \% \quad (2.41)$$

All fits give very stable results for the intensities of these two tensors while varying the $a_0(1450)$-intensity in a wide range :

$$I(f_2(1270)\pi^0 \ in \ K_S^0K_S^0\pi^0) \ = \ (4.4 \pm 0.7) \ \% \quad (2.42)$$
$$I(a_2(1320)\pi^0 \ in \ K_S^0K_S^0\pi^0) \ = \ (4.4 \pm 0.8) \ \% \quad (2.43)$$

The intensity of the $a_2(1320)$ becomes a factor of two larger if the alternative parametrization with two different production rates for the $(K\pi)_S$-wave is used.

From the intensities the branching ratios can be derived :

$$BR(p\overline{p} \ (^1S_0){\rightarrow}f_2(1270)\pi{\rightarrow}K\overline{K}\pi) \ = \ (4.0 \pm 0.6) \times 10^{-4} \quad (2.44)$$
$$BR(p\overline{p} \ (^1S_0){\rightarrow}a_2(1320)\pi{\rightarrow}K\overline{K}\pi) \ = \ (4.0 \pm 0.7) \times 10^{-4} \quad (2.45)$$

a_2(1320) : fit and prediction

The branching ratios of eqs. 2.45 and 2.45 can be compared not only with the results from the channels $K_S^0K_S^0\pi^0$ [38] and $K_L^0K_L^0\pi^0$ [35] but, for the a_2, also with those of the channels $K_L^0K^{\pm}\pi^{\mp}$ [51] and $K_S^0K^{\pm}\pi^{\mp}$ [52]. For the latter two cases the relation

$$I(a_2^{\pm}\pi^{\mp} \ in \ K_{S/L}K^{\pm}\pi^{\mp}) \ / \ I(a_2^0\pi^0 \ in \ K_S^0K_S^0\pi^0) \ = \ 1.4 \pm 0.2 \quad [53] \quad (2.46)$$

has been used.

$$BR(p\overline{p} \ (^1S_0){\rightarrow}a_2(1320)\pi{\rightarrow}K\overline{K}\pi) \ = \ (7.6 \pm 0.9) \times 10^{-4} \quad [35] \quad (2.47)$$
$$BR(p\overline{p} \ (^1S_0){\rightarrow}a_2(1320)\pi{\rightarrow}K\overline{K}\pi) \ = \ (6.5 \pm 1.8) \times 10^{-4} \quad [38] \quad (2.48)$$
$$BR(p\overline{p} \ (^1S_0){\rightarrow}a_2(1320)\pi{\rightarrow}K\overline{K}\pi) \ = \ (4.6 \pm 0.8) \times 10^{-4} \quad [51] \quad (2.49)$$
$$BR(p\overline{p} \ (^1S_0){\rightarrow}a_2(1320)\pi{\rightarrow}K\overline{K}\pi) \ = \ (3.4 \pm 0.9) \times 10^{-4} \quad [52] \quad (2.50)$$

Comparing eqs. 2.41 and 2.43 shows a large discrepancy between the results from the channels $\eta\pi^0\pi^0$ and $K_S^0K_S^0\pi^0$(a factor of 5 !). Any attempt to obtained a good fit with the $a_2(1320)$-intensity fixed at 23 % failed completely $(\Delta(ln(\mathcal{L})) \approx -100)$.

Comparing eq. 2.45 with eqs. 2.47-2.50, however, shows that all results obtained so far from different $KK\pi$ channels are of the same order (approximately within two standard deviations) and they are all a factor of 3-5 lower than predicted from $\eta\pi^0\pi^0$. This discrepancy has to be considered as a general problem between $\eta\pi^0\pi^0$ and $K_S^0K_S^0\pi^0$.

$f_2(1270)$: fit and prediction

As to the $f_2\pi^0$-amplitude the measured intensity (eq. 2.43) is in very good agreement with the prediction from the $3\pi^0$-channel (eq. 2.41).

The mixing angle $\theta_{2^{++}}$ of the 2^{++}-meson nonet can be calculated in the same way as in [35] from the results of the channel $K_L^0 K_L^0 \pi^0$:

$$\frac{BR(p\overline{p} \rightarrow f_2'\pi^0)}{BR(p\overline{p} \rightarrow f_2\pi^0)} = tan^2(\theta_{2^{++}} - 35.3^0) \longrightarrow \theta_{2^{++}} = (24.9 \pm 1.7)^0 \tag{2.51}$$

This result is in very good agreement with $\theta_{2^{++}} = 26^0$ derived from the linear mass formula [1].

Further tensor resonances ?

More tensor resonances as the $f_2(1540)$ or the $a_2(1620)$ are kinematically possible. Any attempt, however, to add an additional tensor to the fit failed. The fact that a fit of mass and width of the $f_2'(1525)$ leads to exact the values form [1] of this particle is a further indication that no other tensor is required by the fit.

2.7 Fits to $K_S^0 K_S^0 \eta$

The phase space of $K_S^0 K_S^0 \eta$ in $p\overline{p}$ -annihilation at rest is extremely narrow. Possible resonances in the $K_S^0 K_S^0$-system are $f_0(975)$, $a_0(980)$, $f_2(1270)$, $a_2(1320)$ and the tail of the $f_0(1370)$, in the $K_S^0 \eta$-system no resonance is possible.

The two tensor resonances are close to threshold and the angular momentum $l = 2$ between the resonance and the recoiling η leads to the respective damping factor in the amplitude. It is therefore no surprise that the fit does not accept the amplitudes of the two tensor resonances.

From the $K_S^0 K_S^0 \pi^0$-channel a contribution of a scalar at threshold could be expected but from the results of $K_S^0 K_S^0 \pi^0$one can estimate that the signal might be compatible with zero within 3σ. It is therefore understandable that no signal is seen in the data and that the fit rejects a scalar amplitude at threshold.

The only possible resonance left is the $f_0(1370)$. The mass of the resonance ($M = 1430 MeV/c^2$) is outside the phase space but as it is shown in fig 2.18 the long tail of this broad object ($\Gamma = 330 MeV/c^2$) is sufficient to describe the data (mass and width of the $f_0(1370)$ are from the fits to $K_S^0 K_S^0 \pi^0$).

It has of course to be pointed out that the statistics in the $K_S^0 K_S^0 \eta$-channel is very low and an enlarged data sample might reveal more structures.

$K_S^0 K_S^0 \eta$: Fit and Data

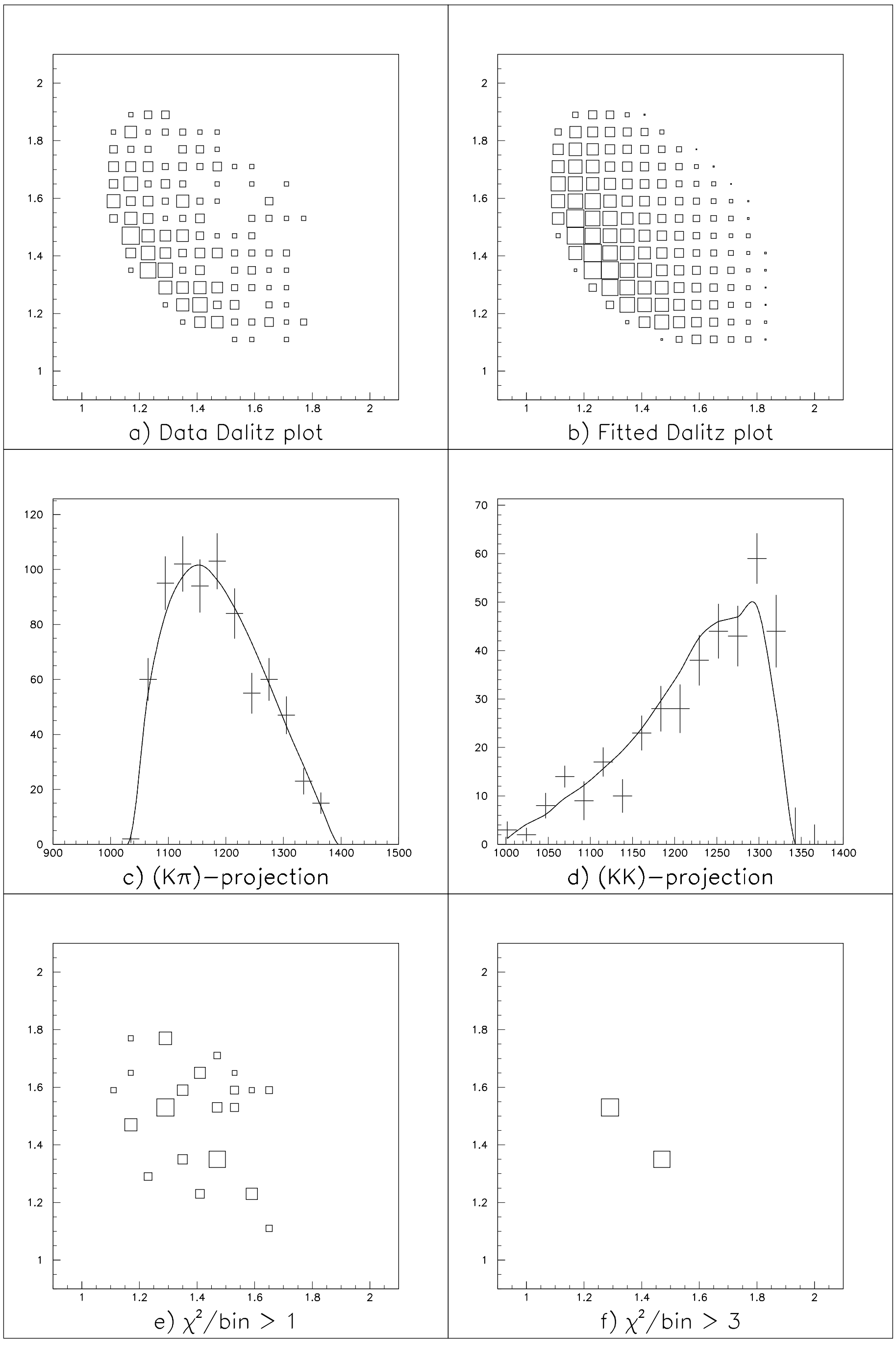

Figure 2.18: *Fit to the $K_S^0 K_S^0 \eta$-data using the $f_0(1370)$ only. Within the error bars the data can be described quite good but the statistics is extremely low.*

Bibliography

[1] L.Montanet et al.: Phys. Rev. D50 (1994) Part I : Review of Particle Properties

[2] F.James, GENBOD N-Body Monte-Carlo Event Generator, CERNLIB W515 (1975)

[3] G. Folger, M. Doser, Ch. Voelcker, Offline Reconstruction Software, CB-Note 121 (1995)

[4] Curtis A. Meyer, LOCATER, Crystal Barrel Charged Tracking Software, CB-Note 123 (1990)

[5] Mark Burchell, Christian Völcker, GTRACK, Crystal Barrel Global Tracking Software, CB-Note 118 (1995)

[6] F.-H. Heinsius, T. Kiel, BCTRAK, Crystal Data Reconstruction Software, CB-Note 92 (1992)

[7] P. Hidas, G. Pinter, CBKFIT, Kinematic Fitting Software, CB-Note 138 (1995)

[8] F.-H. Heinsius, CCDBCB, Crystal Barrel Calibration-Database Software, CB-Note 122 (1991)

[9] R. Brun et al., GEANT3, CERN Report DD/EE/84-1 (1987)

[10] Roy Bossingham, Monte Carlo Software CBGEANT 4.06/03, CB-Note 169 (1992)

[11] A. J. Noble, The Release of CBGEANT 5.00, CB-Note 264 (1994)

[12] P. A. Aarnio et al., Fluka users guide, Technical Report TIS-RP-190, CERN, 1990 (see also GEANT 3.21 manual for further references)

[13] A. J. Noble, A Study of Hadronic Interactions in CBGEANT, CB-Note 258 (1994)

[14] M. Lakata, A New Multi-Vertex Fitter and Updated Vertex-Locater Information, CB-Note 285 rev 1.2 (1996)

[15] P. Hidas, A trick for fitting $K^0_S \rightarrow \pi^0\ \pi^0$ with CBKFIT, Minutes of CB-meeting, Aug 1995

[16] R. McCrady, $p\overline{p} \rightarrow \pi^+\ \pi^-\ \pi^0\ \omega$, Minutes of the Jamboree meeting 03/1996

[17] C. N. Pinder and C. Völcker, Report on the October-November 1993 Crystal Barrel Run, 01/1994

[18] J. Zerbes, Segmentierte Silizium-PIN-Dioden als Strahlzähler für das Crystal Barrel Experiment am CERN, Diplomarbeit, Universität München (1994)

[19] M. Burchell, Analysis Writeup on $BR(\overline{p}p \to \pi^+\pi^-)$, $BR(\overline{p}p \to K^+K^-)$, CB-Note 185, 1992

[20] Bruckner et al., Zeit. für Physik A335 (1990)

[21] N.P. Hessey, Splitoff-recognition with Dolby-C, CB-Note 182, August 1992

[22] M.Benayoun et al., Split-off Recognition in Data with charged Tracks - The TAXI Logics, CB-Note 280, Juni 1995

[23] N.P. Hessey, Calculating Branching Ratios, CB-Note 196, May 1992

[24] S. U. Chung, Spin Formalism, CERN Yellow Report, CERN 71-8 (1971)

[25] S. U. Chung, Formulas for Partial-Wave Analysis, CB Note 211 (1989)

[26] Frank von Hippel and C. Quigg, Phys. Rev. 5, 624 (1972)

[27] C. Amsler et al., Phys. Lett. B355 (1995) 425

[28] S. M. Flatteé, Phys. Letters, 63B (1976) 224

[29] D. V. Bugg et al., Phys. Rev. D 50, number 7 (1994) 4412

[30] D. V. Bugg, A. V. Sarantsev ans B. S. Zou, Nucl. Phys. B471 (1996) 59-89

[31] C. Amsler et al., Phys. Lett. B327 (1994) 425

[32] D. Aston et al., Nucl. Phys. B296 (1988) 491

[33] K. Braune and Chr. Felix, CB-Note 296 (1996)

[34] C. Amsler et al., Phys. Lett. B323 (1994) 233

[35] A. Abele et al., Phys. Lett. B385 (1996) 425

[36] D. Morgan, M. R. Pennington, Phys. Rev. D48 (1993) 1185

[37] I. J. R. Aitchison, Nucl. Phys. A189 (1972) 417

[38] B. Conforto et al., Nucl. Phys. B3 (1967) 469

[39] Chr. Felix, MAXTOOL, Version 96.10 (1996)

[40] C. Amsler and J. C. Bizot, Comp. Phys. Common 30(1983) 21

[41] CERN Program Library Entry D506, MINUIT, Version 92.1 (1992)

[42] S. v. Dombrowski, Proton-Antiproton Annihilation at Rest into π^0 $K_L^0K_L^0$, Technical Report, CB-Note 294, 03/1996

[43] R. Armenteros et al., Phys. Lett. 17(1965) 170

[44] C. Amsler et al., Phys. Lett. B342(1995) 433

[45] C. Amsler, F. E. Close, Phys. Lett. D(1996) 295

[46] A. Abele et al, Nucl. Phys. A609(1996) 562

[47] C. Zupancic, private communication

[48] Techinical Report, Antiproton-Proton Annihilation at Rest into $K_L^0K^\pm\pi^\mp\pi^0$ (Revised Version, Part 4), 1996

[49] D. V. Bugg, private note

[50] C. Amsler et al., Phys. Lett. B335(1995) 425

[51] Bernd Kalteyer, Untersuchung der Proton-Antiproton-Vernichtung in $\pi^\pm K^\mp K_L^0$, Diplomarbeit, Mainz, 1995

[52] Die Proton-Antiproton-Annihilation in $K_S^0K^\pm\pi^\mp$, Diplomarbeit, München, 1996

[53] O. Cramer, Minutes of the CB-meeting, 01/95